MESSENGER and Mariner 10 flyby observations of magnetotail structure and dynamics at Mercury

James A. Slavin,[1] Brian J. Anderson,[2] Daniel N. Baker,[3] Mehdi Benna,[4] Scott A. Boardsen,[1,5] Robert E. Gold,[2] George C. Ho,[2] Suzanne M. Imber,[1,5] Haje Korth,[2] Stamatios M. Krimigis,[2,6] Ralph L. McNutt Jr.,[2] Jim M. Raines,[7] Menelaos Sarantos,[1,6] David Schriver,[8] Sean C. Solomon,[9] Pavel Trávníček,[10] and Thomas H. Zurbuchen[7]

Received 1 June 2011; revised 19 October 2011; accepted 14 November 2011; published 28 January 2012.

[1] The first (M1), second (M2), and third (M3) MESSENGER flybys of Mercury traversed the planet's magnetotail from 1.25 to 3.25 R_M downstream of the planet, where R_M is Mercury's radius (2440 km). The encounters took place under northward, southward, and variable-polarity interplanetary magnetic field (IMF), respectively. The magnetic field strength B in Mercury's magnetotail follows a power law decrease with increasing antisunward distance $|X|$, $B \sim |X|^G$, with G varying from -5.4 for northward to -1.6 for southward IMF. Low-latitude boundary layers (LLBLs) containing strong northward magnetic field were detected at the tail flanks during two of the flybys. The observed thickness of the LLBL was ~33% and 16% of the radius of the tail during M1 and M3, respectively, but the boundary layer was completely absent during M2. Clear signatures of tail reconnection are evident in the M2 and M3 magnetic field measurements. Plasmoids and traveling compression regions were observed during M2 and M3 with typical durations of ~1–3 s, suggesting diameters of ~500–1500 km. Overall, the response of Mercury's magnetotail to the steady southward IMF during M2 appeared very similar to steady magnetospheric convection events at Earth, which are believed to be driven by quasi-continuous reconnection. In contrast, the M3 measurements are dominated by tail loading and unloading events that resemble the large-scale magnetic field reconfigurations observed during magnetospheric substorms at Earth.

Citation: Slavin, J. A., et al. (2012), MESSENGER and Mariner 10 flyby observations of magnetotail structure and dynamics at Mercury, *J. Geophys. Res.*, *117*, A01215, doi:10.1029/2011JA016900.

1. Introduction

[2] The flybys of Mercury by the Mariner 10 and MErcury Surface, Space ENvironment, GEochemistry, and Ranging (MESSENGER) spacecraft have shown that the planet's internal magnetic field is largely dipolar, aligned with the spin axis, and of the same polarity as Earth's field [*Anderson et al.*, 2008, 2010; *Alexeev et al.*, 2008, 2010]. The field's interaction with the solar wind causes a portion of Mercury's magnetic field to be swept downstream to form a planetary magnetotail [*Russell et al.*, 1988]. Initial analyses of the MESSENGER measurements showed that the magnetic fields in Mercury's tail varied greatly from one flyby to the next and to exhibit dynamic variations on time scales of seconds to minutes [*Slavin et al.*, 2008, 2009, 2010b].

[3] Previous studies of Mercury's magnetosphere have indicated that the direction of the interplanetary magnetic field (IMF) is the dominant factor determining the intensity of plasma convection in Mercury's magnetosphere through the effects of magnetic reconnection [*Baker et al.*, 1986; *Russell et al.*, 1988; *Slavin*, 2004; *Baumjohann et al.*, 2006; *Fujimoto et al.*, 2007]. This conclusion has been supported by extensive magnetohydrodynamic [*Kabin et al.*, 2000; *Ip*

[1]Heliophysics Science Division, NASA Goddard Space Flight Center, Greenbelt, Maryland, USA.
[2]Johns Hopkins University Applied Physics Laboratory, Laurel, Maryland, USA.
[3]Laboratory for Solar and Atmospheric Physics, University of Colorado at Boulder, Boulder, Colorado, USA.
[4]Solar System Exploration Division, NASA Goddard Space Flight Center, Greenbelt, Maryland, USA.
[5]Also at Goddard Earth Science and Technology Center, University of Maryland, Baltimore County, Baltimore, Maryland, USA.
[6]Also at Office of Space Research and Technology, Academy of Athens, Athens, Greece.
[7]Department of Atmospheric, Oceanic and Space Sciences, University of Michigan, Ann Arbor, Michigan, USA.
[8]Institute for Geophysics and Planetary Physics, University of California, Los Angeles, California, USA.
[9]Department of Terrestrial Magnetism, Carnegie Institution of Washington,Washington, DC, USA.
[10]Astronomical Institute, Academy of Sciences of the Czech Republic, Prague, Czech Republic.

0148-0227/12/2011JA016900

and Kopp, 2002; *Kidder et al.*, 2008; *Benna et al.*, 2010] and hybrid simulations [*Janhunen and Kallio*, 2004; *Trávníček et al.*, 2010; *Wang et al.*, 2010] of Mercury's magnetosphere. Magnetic reconnection occurs at the dayside magnetopause of Earth when there is a component of the IMF that is antiparallel to the subsolar magnetospheric magnetic field. Analysis of MESSENGER magnetic field measurements has shown this also to be the case at Mercury [*Slavin et al.*, 2009, 2010a; *Anderson et al.*, 2011]. Indeed, the rate of reconnection at Mercury's magnetopause has been determined to be ~10 times that typical at Earth [*Slavin et al.*, 2009], most probably a result of the low solar wind Alfven Mach number and values of plasma β, the ratio of plasma thermal pressure to magnetic pressure, typical of the inner heliosphere [*Slavin and Holzer*, 1979; *Fujimoto et al.*, 2007]. Dayside reconnection at Earth loads the tail lobes with magnetic flux and increases the tail's overall energy levels, which are later dissipated in tail reconnection and substorms [*Caan et al.*, 1973]. Such loading of the magnetotail with magnetic flux has also been observed at Mercury, but with the fractional enhancement in the lobe magnetic field much larger than what is observed at Earth, i.e., by up to a factor of 2 [*Slavin et al.*, 2010b] rather than by 10 to 30% as at Earth [*Milan et al.*, 2004; *Huang and Cai*, 2009].

[4] The magnetic fields in the northern and southern lobes of planetary magnetotails are oppositely directed and, therefore, always properly oriented for reconnection to occur. However, the magnetic field normal to the cross-tail current layer has a stabilizing effect and inhibits reconnection, especially when the lobe magnetic fields are weak. Tail loading increases the magnetic flux in the lobe and, in turn, tail flaring. This enhanced flaring increases the fraction of solar wind ram pressure applied to the tail and leads to thinning of the plasma sheet and its embedded cross-tail current layer [*Kuznetsova et al.*, 2007; *Winglee et al.*, 2009; *Raeder et al.*, 2010]. Current sheet thinning reduces the normal magnetic field component to the point where it becomes unstable to reconnection. Fast magnetic field reconfiguration and dissipation then ensue with the liberated energy powering rapid magnetospheric convection, plasma heating, energetic particle acceleration, and other phenomena [*McPherron et al.*, 1973; *Hones et al.*, 1984; *Baker et al.*, 1996].

[5] A fundamental, but not well understood, aspect of the reconnection process is the formation of magnetic islands with helical or quasi-looplike topologies in the cross-tail current layer [*Hesse and Kivelson*, 1998]. These magnetic structures are called "plasmoids" [*Hones et al.*, 1984]. Because of their high speed and large dimensions relative to the surrounding plasma sheet, they locally compress the lobe magnetic field draped about the plasmoid. These compressions accompany the plasmoid as it moves sunward or antisunward. For this reason they are termed "traveling compression regions" (TCRs) [*Slavin et al.*, 1993]. TCRs can be observed over a large fraction of the lobe region, and they are, therefore, observed far more frequently than the underlying plasmoids that occupy a much smaller volume. Plasmoids and TCRs are known to be highly correlated not only with reconnection in the tail, but also with the onset of magnetospheric substorms [*Moldwin and Hughes*, 1992; *Slavin et al.*, 1992; *Baker et al.*, 1996]. Many flux ropes or magnetic loops can be formed during a given reconnection event, with some being carried sunward and others tailward by the fast Alfvenic jetting of plasma away from reconnection *X* lines [*Slavin et al.*, 2003, 2005]. Indeed, initial analyses of the MESSENGER measurements have revealed the presence of sunward and antisunward moving plasmoids and TCRs at Mercury [*Slavin et al.*, 2009, 2010b].

[6] The circulation of plasma, magnetic flux, and energy from the *X* line at the dayside magnetopause to the *X* line in the nightside cross-tail current layer constitutes the "Dungey cycle" that powers Earth-type magnetospheres [*Dungey*, 1961; *Cowley*, 1982]. The Dungey cycle time at Earth is ~1 h [*Cowley*, 1982], but at Mercury it is only ~1–2 min [*Siscoe et al.*, 1975; *Slavin et al.*, 2009]. However, much remains to be understood regarding the system-wide response of magnetospheres to reconnection and the role of upstream "drivers," including IMF direction and such internal conditions as ionospheric conductance. A steady southward component of the IMF at Earth (i.e., antiparallel to the subsolar planetary magnetic field) is sometimes observed to drive periods of enhanced, but steady, magnetospheric convection, termed steady magnetospheric convection (SMC) events [S*ergeev et al.*, 1996; *Tanskanen et al.*, 2005; *McPherron et al.*, 2005]. In contrast, intervals of southward IMF of variable intensity and duration tend to load the tail with magnetic flux transferred from the dayside magnetosphere [*McPherron et al.*, 1973; *Caan et al.*, 1973]. This newly opened magnetic flux is stored in the lobes for a time on the order of the Dungey cycle time and then dissipated (i.e., closed and returned to the forward magnetosphere) by reconnection in the tail [*Milan et al.*, 2004]. The factors determining the length of time that magnetic fields may be stored in the tail and the cause or "trigger" for the onset of unloading, however, remain elusive [*Henderson et al.*, 1996; *Lyons et al.*, 1997; *Hsu and McPherron*, 2004; *Liou*, 2007]. These episodes of intense reconnection-driven convection that unload the tail are termed magnetospheric substorms [*Baker et al.*, 1996]. Although terrestrial-style substorms involving auroras and the close coupling between an electrically conducting ionosphere and a magnetosphere cannot take place at Mercury, Mariner 10, and MESSENGER observations of rapid variations in the tail magnetic fields accompanied by plasmoid ejection and charged particle acceleration are collectively termed "substorms" as well [*Siscoe et al.*, 1975; *Slavin et al.*, 2010b].

[7] Here we analyze MESSENGER observations of Mercury's magnetotail during intervals of northward, southward, and variable-polarity IMF. The structure of the magnetotail is examined and found to be similar to that of Earth. The response of Mercury's magnetotail to continuous southward IMF is found to be similar to steady magnetospheric convection events at Earth. In contrast, variable-polarity IMF produces rapid, large-amplitude reconfigurations of the magnetospheric magnetic field very similar to those observed during terrestrial magnetospheric substorms.

2. Mariner 10 and MESSENGER Flyby Trajectories

[8] The trajectories of the Mariner 10 flybys of 29 March 1974 (MI) and 16 March 1975 (MIII) and the MESSENGER flybys of 14 January 2008 (M1), 6 October 2008 (M2), and 29 September 2009 (M3) are depicted in Figure 1. The mean

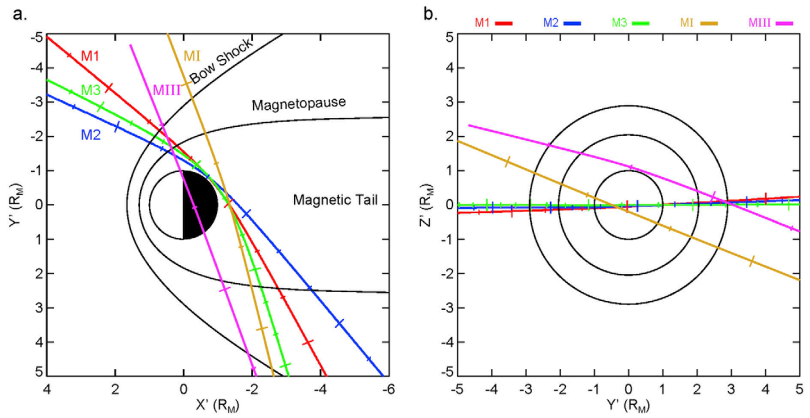

Figure 1. Projections of the MI (2020–2110 UTC), MIII (2220–2300 UTC), M1 (1820–1950 UTC), M2 (0745–0915 UC), and M3 (2100–2140 UTC) trajectories (tic marks every 10 min) in the solar wind aberrated (a) MSO $X'-Y'$ and (b) MSO $Z'-Y'$ planes. UTC denotes Coordinated Universal Time.

bow shock and magnetopause surfaces shown are those derived from the boundary crossings observed during the five flybys [*Slavin et al.*, 2010b]. The three MESSENGER flybys are notable for lying very close to the plane of Mercury's orbit. In contrast, MI was moderately inclined and passed through Mercury's orbital plane very near closest approach, whereas MIII was a very high-latitude flyby near the terminator plane. Data taken during this latter Mariner 10 flyby will not be used in this study. Taken together, the observations during MI, M1, M2, and M3 provide good coverage of the dusk side of Mercury's magnetotail between $X_{MSO} \sim -1.25$ and -3.25 R_M, where R_M is Mercury's radius. Mercury solar orbital (MSO) coordinates are used in this paper for both the magnetic field (B_X, B_Y, B_Z) and spacecraft position (X_{MSO}, Y_{MSO}, Z_{MSO}). In MSO coordinates X_{MSO} is directed from the center of the planet toward the Sun, Z_{MSO} is normal to Mercury's orbital plane and positive toward the north celestial pole, and Y_{MSO} is positive in the direction opposite to orbital motion. MESSENGER's orbit about Mercury is expected to be relatively fixed in inertial space with an 82.5° inclination and an initial periapsis latitude near 60°N. As Mercury orbits the Sun during the course of its 88 day year, MESSENGER's orbit will cross the equatorial plane and sample the low-latitude

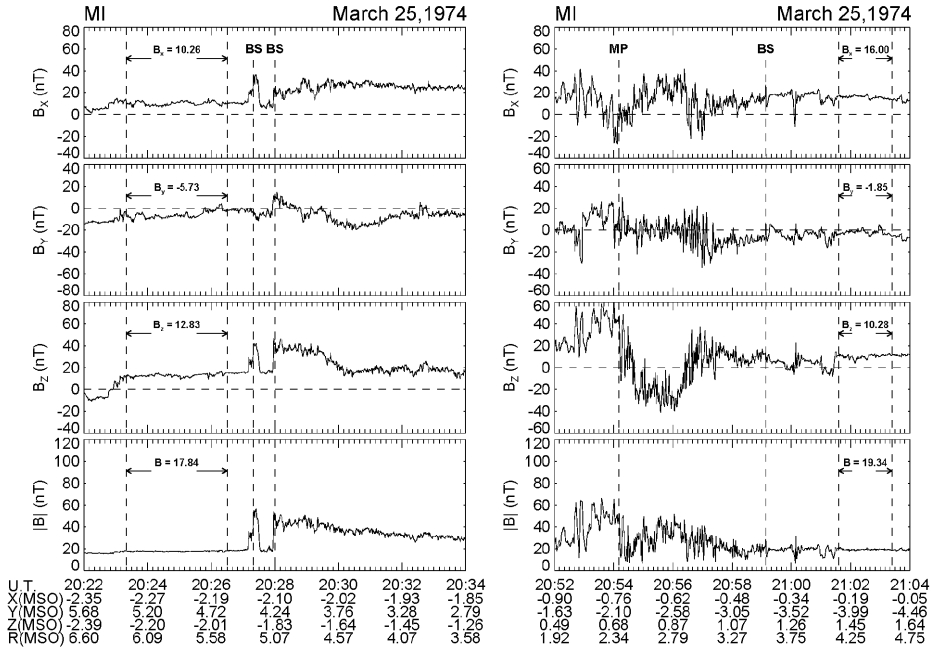

Figure 2. Mariner 10 magnetic field measurements (1.2/s) taken during MI. The occurrence of bow shock (BS) crossings and intervals upstream of the bow shock that have been used to obtain average IMF values are marked with vertical dashed lines and labels. Note the strong, relatively steady northward interplanetary magnetic field (IMF) just prior to the inbound bow shock and magnetotail passage. In contrast, Mariner 10 observed at least a several-minute-long interval of southward IMF just as it crossed the magnetopause (MP) into the magnetosheath.

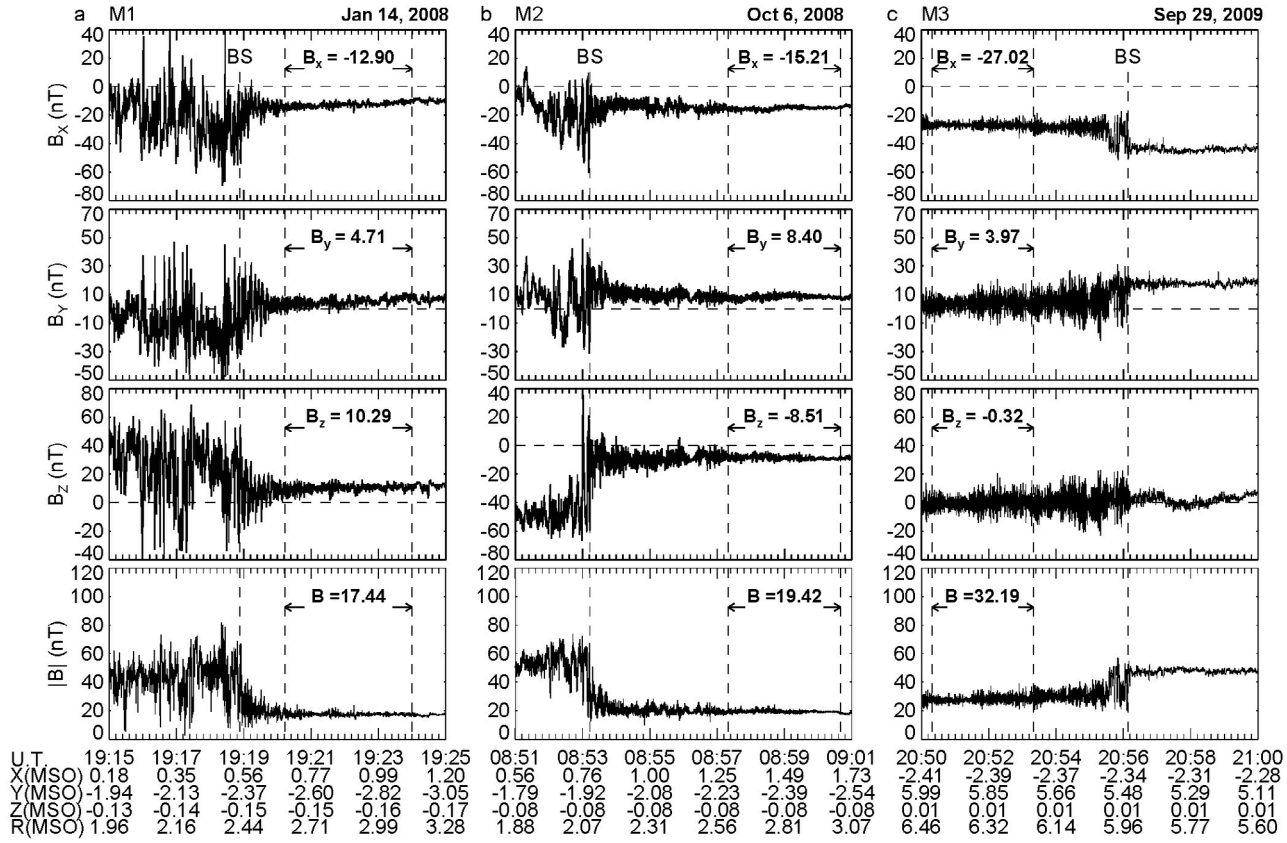

Figure 3. MESSENGER magnetic field measurements (20/s) taken during intervals containing the (a) outbound M1, (b) outbound M2, and (c) inbound M3 bow shock crossings. Mean values for the magnetic field just upstream of the bow shock averaged over the interval between the vertical dashed lines are displayed.

magnetosphere at only two radial distances from the center of Mercury, ~1.5 and 3 R_M [*Solomon et al.*, 2001].

[9] In addition to MSO coordinates it is useful to define coordinates, denoted here by primes, that are aberrated (i.e., rotated) by a small angle so that the X'_{MSO} axis is antiparallel to the mean solar wind flow direction in Mercury's rest frame. For the purpose of aberrating the Mariner 10 and MESSENGER measurements the solar wind is assumed to be radial outward from the Sun, and the best available estimates of solar wind speed [*Ogilvie et al.*, 1977; *Baker et al.*, 2009, 2011] are used, as described in the next section.

3. Interplanetary Conditions

[10] Magnetic field measurements [*Ness et al.*, 1974] taken just before (after) the inbound (outbound) bow shock encounters during MI are displayed in Figure 2. As shown, this encounter began with relatively steady northward IMF B_Z, but ended with southward magnetic fields observed immediately upon exit through the magnetopause into the magnetosheath. Because of the quiet nature of the tail magnetic field before closest approach and the large amplitude of the fluctuations that commenced afterward, it has been hypothesized that the IMF turned southward near the time that Mariner 10 first encountered the dipolar magnetic field near the planet [*Siscoe et al.*, 1975; *Ogilvie et al.*, 1977].

[11] Magnetic field measurements [*Anderson et al.*, 2007] taken by MESSENGER in the vicinity of the outbound bow shock during M1 and M2 and the inbound bow shock during M3 (no measurements were taken following closest approach during M3 because the power system software triggered a safe hold that stopped instrument data collection [*Slavin et al.*, 2010b]), are shown in Figure 3. The outbound IMF observations are preferred here because they are taken only a few minutes after the outbound magnetopause observations, whereas the inbound bow shock crossings are more than an hour before the inbound magnetopause crossings. Hence, the outbound IMF is more representative of that during the magnetospheric passage than the inbound IMF [*Korth et al.*, 2011]. As displayed, the IMF was steadily northward during M1 [*Anderson et al.*, 2008] and steadily southward for M2 [*Slavin et al.*, 2009]. M3 was different in that IMF B_Z was on average near zero but meandered northward and then southward on time scales of minutes in the magnetosheath during the period leading up to the magnetopause crossing [*Slavin et al.*, 2010b]. The IMF during M3 was about 32 nT or nearly twice that of the other flybys. For all three MESSENGER flybys the radial or B_X component of the IMF was dominant because the typical Parker spiral angle (i.e., the angle that the IMF makes to the radial direction from the Sun) is only ~20° at Mercury orbit [*Korth et al.*, 2011].

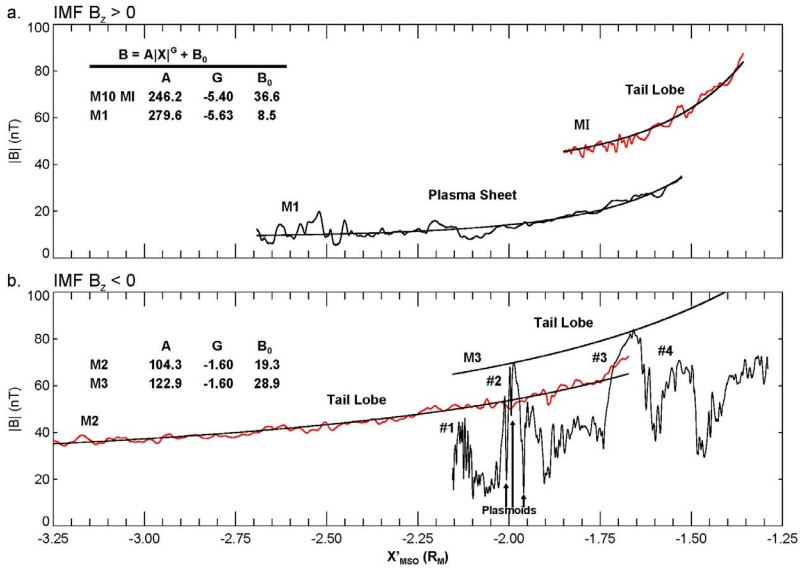

Figure 4. (a) Magnetic field magnitude in the tail lobe and plasma sheet measured during the first Mariner 10 (0.04 s resolution) and MESSENGER (0.05 s resolution) flybys, respectively, which took place during northward IMF, as functions of X'_{MSO}. (b) Similar display for the second and third MESSENGER tail passages, which took place during southward and mixed northward/southward IMF conditions, respectively. Best fits to the decrease in field magnitude with increasing distance down the tail are indicated; for M3, the fit is only to the peaks in the field magnitude.

[12] The upstream solar wind speed and density for the first Mariner 10 flyby were estimated to be 550 km/s and 14 cm^{-3} on the basis of in situ electron measurements [*Ogilvie et al.*, 1977]. MESSENGER carries a Fast Imaging Plasma Spectrometer (FIPS), but its primary purpose is the determination of planetary ion composition and its location behind the spacecraft sunshade precludes regular solar wind measurements [*Zurbuchen et al.*, 2008; *Raines et al.*, 2011]. However, ground-based magnetograph measurements of solar magnetic field have been used to estimate solar wind speed, density, and temperature for the MESSENGER flybys using the well validated Wang-Sheeley-Arge (WSA) simulation model [*Baker et al.*, 2009, 2011]. The solar wind parameters inferred in this manner for M1, M2, and M3 are 420 km/s, 60 cm^{-3}, and 1.2×10^5 K; 380 km/s, 60 cm^{-3}, and 2.0×10^5 K; and 390 km/s, 50 cm^{-3}, and $T = 1.0 \times 10^5$ K, respectively.

4. Magnetic Field Variation Down the Tail

[13] The magnetic field intensity in planetary magnetotails decreases with increasing distance down the tail [*Slavin et al.*, 1985; *Kivelson and Khurana*, 2002; *Jackman and Arridge*, 2011]. In the absence of comprehensive plasma measurements, magnetic field measurements in the tail are classified as being characteristic of the "lobe" or "plasma sheet" regions on the basis of field intensity, direction, and level of fluctuations. This approach has been used frequently with good results and is described in more detail elsewhere [e.g., *Slavin et al.*, 1985]. Briefly, steady, strong magnetic fields, relative to the draped IMF in the magnetosheath, oriented generally toward or away from Mercury are identified as lobe regions, whereas weaker, more variable magnetic fields in Mercury's wake are classified as plasma sheet regions for the analysis of the gross morphology of the tail magnetic field.

[14] The decrease in tail field intensity with distance occurs because the outward flaring of the magnetopause decreases with increasing distance as the tail becomes more cylindrical [*Coroniti and Kennel*, 1972]. In the plasma sheet the situation is complicated by the fact that the thermal pressure of the plasma is generally much greater than the magnetic pressure and the gradient in the plasma pressure down the tail is balanced by the sunward $\mathbf{J} \times \mathbf{B}$ force in the cross-tail current layer, where $\mathbf{J}$ is the current. However, a power law decrease in magnetic field intensity B with downstream distance $|X|$ nonetheless fits the tail magnetic fields in both regions well:

$$B(X) = A|X|^G + B_0, \tag{1}$$

where B_0 is the asymptotic distant tail field. For example, the Earth lobe field decreases from $X \sim -20$ to -200 R_E (where R_E is Earth's radius) as $G \sim -0.5$ until a terminal diameter of $\sim$60 R_E is reached at $X \sim -100$ R_E where $B_0 \sim 10$ nT [*Slavin et al.*, 1985]. Balance between the magnetic pressure in the lobes and the magnetic and thermal plasma pressure in the interplanetary medium implies, under the assumption that the magnetic and plasma pressures are similar, that the terminal lobe magnetic field intensity is approximately equal to $\sqrt{2}$ or $\sim$1.4 times the IMF strength. The values of B_0 expected for MI, M1, and M2 by this scaling argument are $\sim$25–30 nT, whereas the strong IMF during M3 implies $B_0 \sim 46$ nT.

[15] Magnetic field intensity measured as a function of X'_{MSO} at times of northward IMF B_Z are compared for MI and M1 in Figure 4a. Figure 4b displays the analogous MESSENGER M2 land M3 measurements taken when IMF

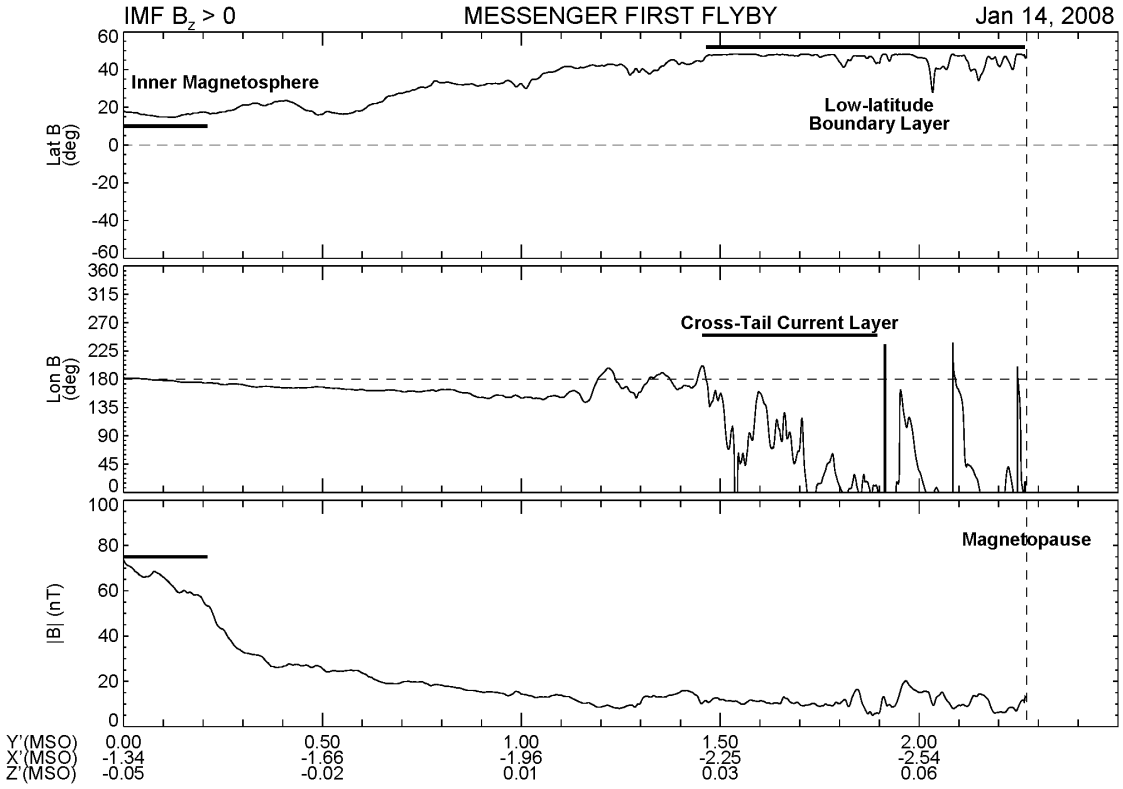

Figure 5a. Magnetic field measurements during M1 (1 s averages) plotted against the aberrated Y'_{MSO} coordinate of spacecraft position during its traversal of the dusk-side magnetotail. The time interval spanned is 1843:02 to 1859:39 UTC. (top) Latitude angle of the field (north is +90°). (middle) Longitude of the field relative to the sunward (0°) and antisunward (180°) directions. (bottom) Magnetic field intensity. Horizontal bars mark both the highly inclined magnetic fields in the low-latitude boundary layer on the duskward flank of the tail and the strong magnetic fields in the inner magnetosphere closer to Mercury near local midnight.

B_Z was steadily southward and of variable polarity, respectively. The MI and M2 measurements were taken in the tail lobes [*Ness et al.*, 1974; *Slavin et al.*, 2009]. The M3 measurements were also primarily collected in the lobes, but the tail appears to have been undergoing strong temporal variations in the form of four large-amplitude tail loading and unloading events [*Slavin et al.*, 2010b]. Least squares power law fits to these data show that the decrease with planetary distance for MI is much faster, $G = -5.4$, than the $G = -1.6$ determined for M2. The temporal variations in the M3 measurements preclude a single fit to all of the measurements, but, as shown in Figure 4b, a $G = -1.6$ curve with B_0 = 28.9 nT does produce a physically reasonable fit to the peak loading intervals in the M3 data. For MI and M2, the estimated values of the terminal lobe field B_0 of 37 and 19 nT straddle the expected value of ~25–30 nT scaled from IMF intensity, respectively.

[16] The large difference in the G values between MI and M2–M3 is likely due to the very different IMF B_Z conditions under which the measurements were collected. For northward IMF the tail flux content is expected to be lower, the rate of magnetic field decrease more rapid, and the location at which tail flaring ceases closer to the planet [*Coroniti and Kennel*, 1972; *Macek and Grzedzielski*, 1986]. The faster decrease in magnetic field intensity for MI, $G = -5.4$, under IMF $B_Z > 0$ compared with the slower decrease, $G = -1.6$, for M2 and M3 under $B_Z < 0$, is consistent with this expectation. Fits to the near-tail magnetic field at Earth at scaled distances close to those for the MESSENGER flybys produce G values of −3.4 to −0.9 [*Nakai et al.*, 1999], which are similar to those obtained here. The M1 measurements in Figure 4a differ in that they appear to have been taken in the central plasma sheet [*Slavin et al.*, 2008]. Like the MI flyby measurements, the first MESSENGER flyby data were also collected during IMF $B_Z > 0$. The weakness of the M1 magnetic fields is readily attributed to the high plasma pressure in the plasma sheet. The rapid decrease in magnetic field intensity for M1, $G = -5.6$, is similar to the rate determined for MI under similarly northward IMF.

5. Magnetic Field Variation Across the Tail

[17] Inspection of the trajectory plots indicates that the MESSENGER data also provide information regarding how Mercury's magnetic field varies across the magnetotail (i.e., from dusk to dawn). Figure 5a displays the M1 magnetic field measurements as a function of Y'_{MSO}. The plot spans the region from the inbound magnetopause crossing at 1843:02 UTC to local midnight. The magnetic field immediately inside the tail was northward and weak relative to

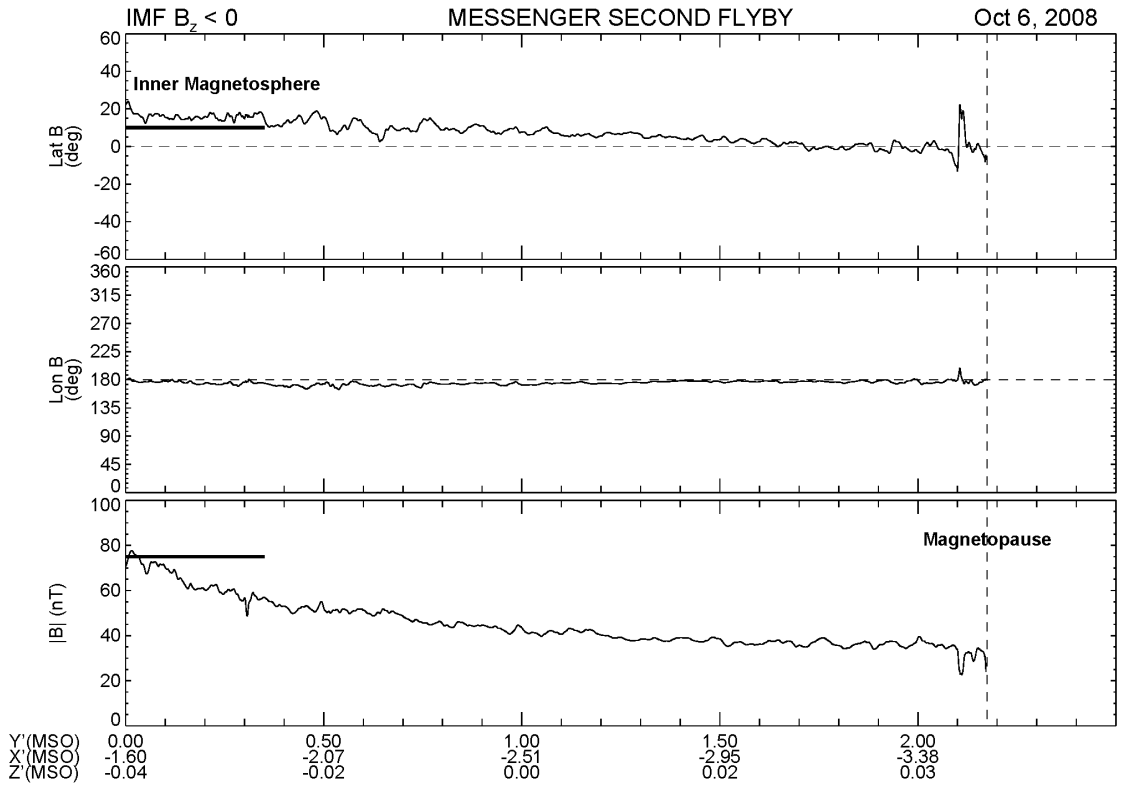

Figure 5b. Magnetic field measurements during M2 displayed in the same format as Figure 5a. The time interval spanned is 0811:58 to 0832:13 UTC.

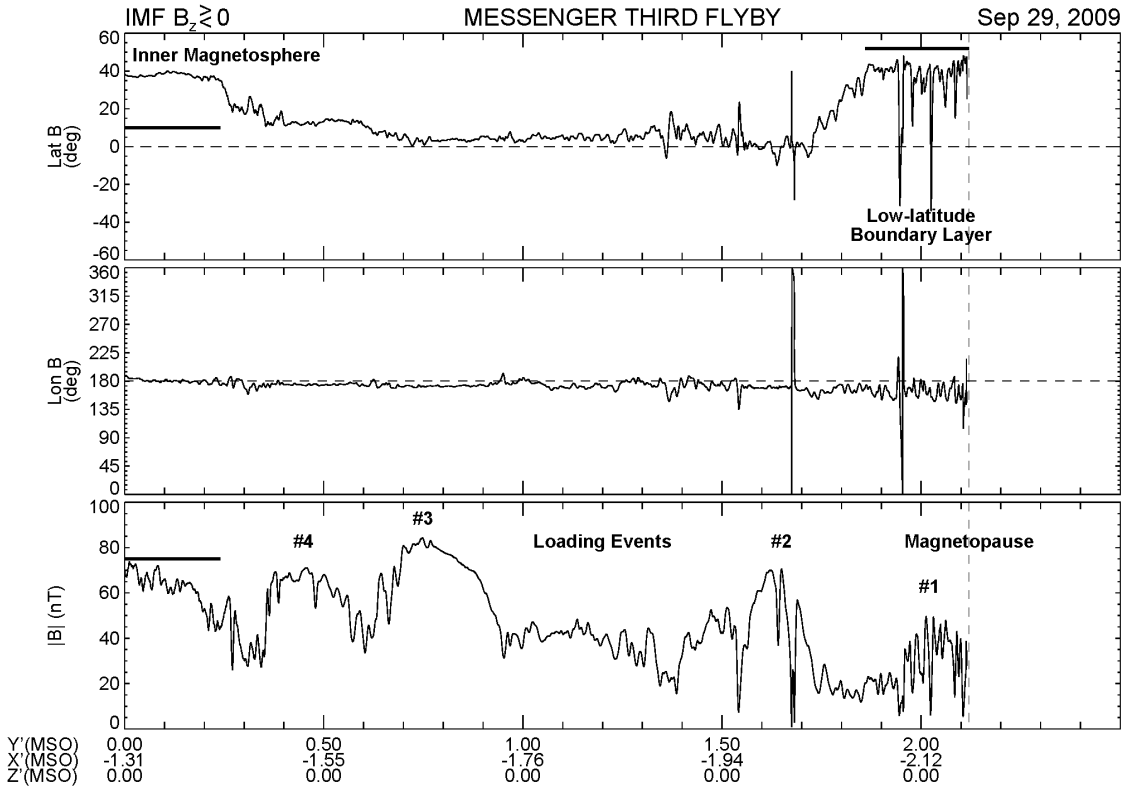

Figure 5c. Magnetic field measurements during M3 displayed in the same format as Figure 5a. The time interval spanned is 2127:45 to 2148:17 UTC.

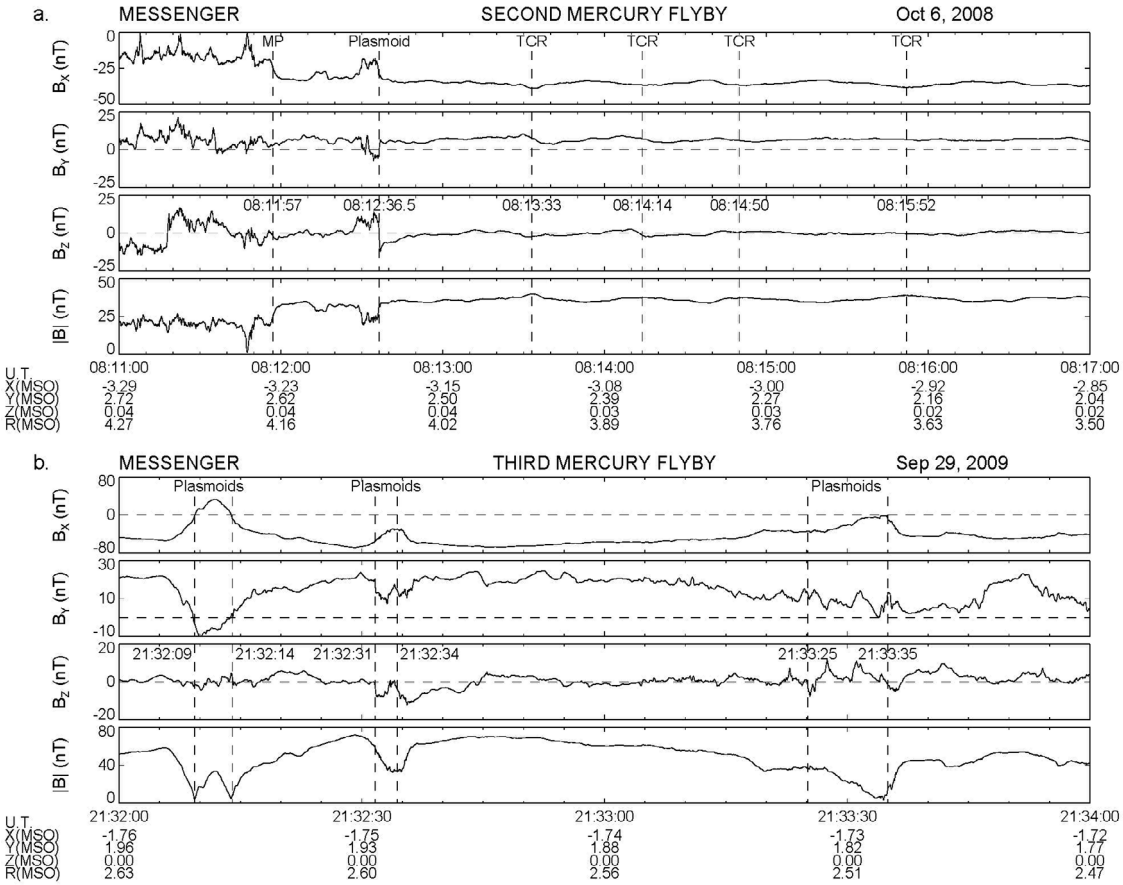

Figure 6. MESSENGER magnetic field measurements (1 s averages) taken during portions of (a) M2 and (b) M3 showing NS plasmoids and TCRs (indicated with vertical dashed lines).

the field in the external magnetosheath, indicating that MESSENGER was located deep in the central plasma sheet and the cross-tail current layer [*Slavin et al.*, 2008]. Immediately thereafter the longitude angle of the magnetic field rotated through 180° twice, between 1843 and 1846 UTC, during what may have been an incipient Kelvin-Helmholtz boundary wave encounter [*Slavin et al.*, 2008; *Sundberg et al.*, 2010]. The magnetic field then gradually rotated from sunward (longitude 0°) to antisunward (180°) as MESSENGER moved through the cross-tail current layer between 1847 and 1849 UTC.

[18] Special attention is called to the steady latitude angle of 45°–50° over a length scale of 0.8 R_M, or $\sim 2 \times 10^3$ km, inward from the magnetopause. This same phenomenon in the low-latitude magnetic field at the flanks of the tail is observed at Earth, and it is termed the low-latitude boundary layer (LLBL) [*Fairfield*, 1979; *Slavin et al.*, 1985; *Kaymaz et al.*, 1994]. The magnetotail LLBL is believed to be the tailward extension of the low-latitude boundary layer that forms just inside the dayside magnetopause [*Hones et al.*, 1972; *Cowley*, 1982; *Mitchell et al.*, 1987].

[19] The analogous magnetic field measurements during M2 are presented in Figure 5b. These observations, which were made during an interval with steady southward IMF B_Z, show no indication of an LLBL at the flank of the tail. The latitude angle of the magnetic field was small all across the tail, consistent with a tail magnetic field that was highly stretched and a plasma sheet that was highly thinned [*Slavin et al.*, 2009]. In contrast, the magnetic field measurements during M3 displayed in Figure 5c show a clear but narrow LLBL at the dusk flank of the tail. The width of the region of strongly northward directed magnetic fields, with latitude angles of $\sim$40°–45°, is about 0.25 R_M or 1×10^3 km. The M3 LLBL region extended beyond the very strong Kelvin-Helmholtz boundary wave activity that accompanied the first tail-loading event [*Slavin et al.*, 2010b; *Boardsen et al.*, 2010]. The time history of the IMF B_Z component while MESSENGER was in Mercury's magnetotail is not known, but the existence of strong tail-loading events implies that the IMF continued to vary between northward and southward tilting on time scales of $\sim$1–10 min as it had for some time prior to entry into the tail [*Slavin et al.*, 2010b].

6. Plasmoids and Traveling Compression Regions

[20] A plasmoid can be seen in magnetic field measurements taken between 0811 and 0817 UTC during M2 (Figure 6a). The plasmoid, which occurred shortly after the magnetopause crossing at 0811:57 UTC, is indicated by the north-then-south variation in the magnetic field followed by a longer recovery back to $B_Z \sim 0$ [*Slavin et al.*, 2009]. The time between extrema of the $\pm B_Z$ signatures, marking the boundaries of the plasmoid, is about 4 s. Beginning 58 s later, a series of four brief compressions of the lobe magnetic

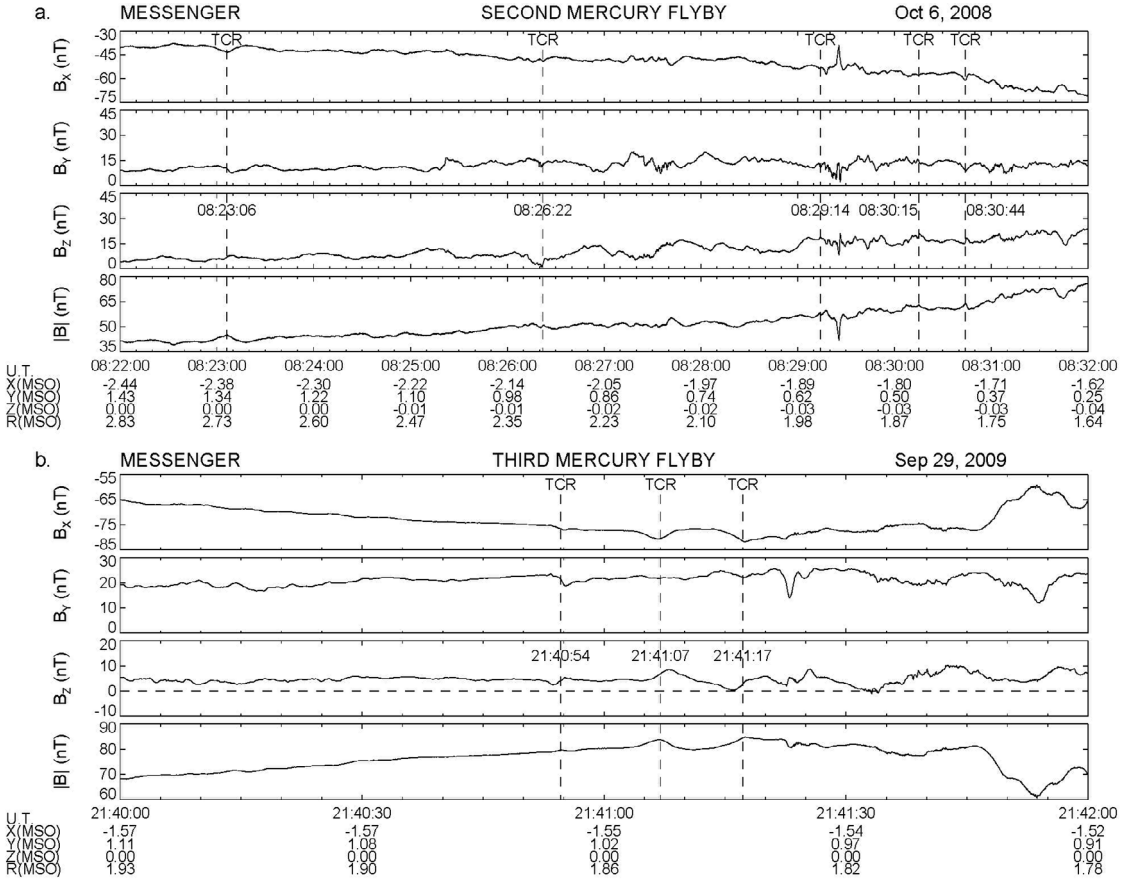

Figure 7. MESSENGER magnetic field measurements (1 s averages) taken during intervals from (a) M2 and (b) M3 containing SN TCRs (indicated with vertical dashed lines).

field were observed between 0813:30 and 0817:00 UTC at intervals of 30–62 s. Each compression was accompanied by north-then-south (NS) tilting of the magnetic field. These several-second-long events are all NS-traveling compression regions caused by the draping of the lobe magnetic field about plasmoids as they are ejected down the tail. The east-then-west field-line draping accompanying some of the events indicates that the underlying plasmoids extended to greater $\pm Z_{MSO}$ values duskward of MESSENGER (e.g., see the discussion of three-dimensional draping by *Slavin et al.* [1993]). During the time interval spanned by the M2 plasmoid and NS TCRs the intensity of the tail magnetic field was relatively constant at ~30–35 nT. Hence, the rate of magnetic flux addition to the tail by reconnection at the dayside magnetopause must have been in approximate balance with the rate of flux removal by tail reconnection and the plasmoid ejection process.

[21] Further examples of plasmoids may be seen in magnetic field measurements obtained during M3, from 2132 to 2134 UTC, within a 2 min period centered on the second tail-loading event [*Slavin et al.*, 2010b] (see Figure 6b). Three pairs of several-second-long plasmoids are identified on the basis of their north-then-south B_Z signatures followed by a slower recovery back to $B_Z \sim 0$. The close proximity of the plasmoids in each pair with a separation comparable to their duration suggests that they formed in parallel due to reconnection at multiple simultaneous X lines [*Slavin et al.*, 2005]. The amplitude of the north-south field variation is weakest for the first pair and strongest in the final pair. The time spacing between successive pairs of plasmoids was ~20 and 60 s. These events mark the transition from loading to unloading, with the magnetic field steadily decreasing after the middle pair of plasmoids.

[22] Five TCRs may be seen during a 10 min segment of magnetic field data from M2 (Figure 7a) spanning 0822 to 0832 UTC at positions between $X' \sim -2.4$ and -1.7 R_M. The events are similar to the TCRs in Figure 6a, except that the sense of the B_Z draping pattern is south–then–north (SN), indicating that they are associated with sunward-moving plasmoids [*Slavin et al.*, 2005]. The TCRs occurred at 0823:06, 0826:22, 0829:14, 0830:15, and 0830:44 UTC, respectively. The time between events was less regular than for the earlier plasmoids and TCRs, but the spacing between the last three events was, again, ~30–60 s. Three additional SN TCRs can be seen within 2 min of M3 magnetic field measurements from 2140 to 2142 UTC centered on the third M3 tail-loading event (Figure 7b). The three TCRs were close in time to each other at 2140:54, 2141:07, and 2141:17 UTC, in a temporal pattern similar to that of the plasmoid pairs during the second tail-loading event (Figure 6b).

[23] A superposed epoch analysis of the one M2 and six M3 plasmoids is presented in Figure 8a. In this analysis the zero epoch is the taken to be the midpoint in the B_Z variation. The average B_Z waveform shows a ~2–3 s long

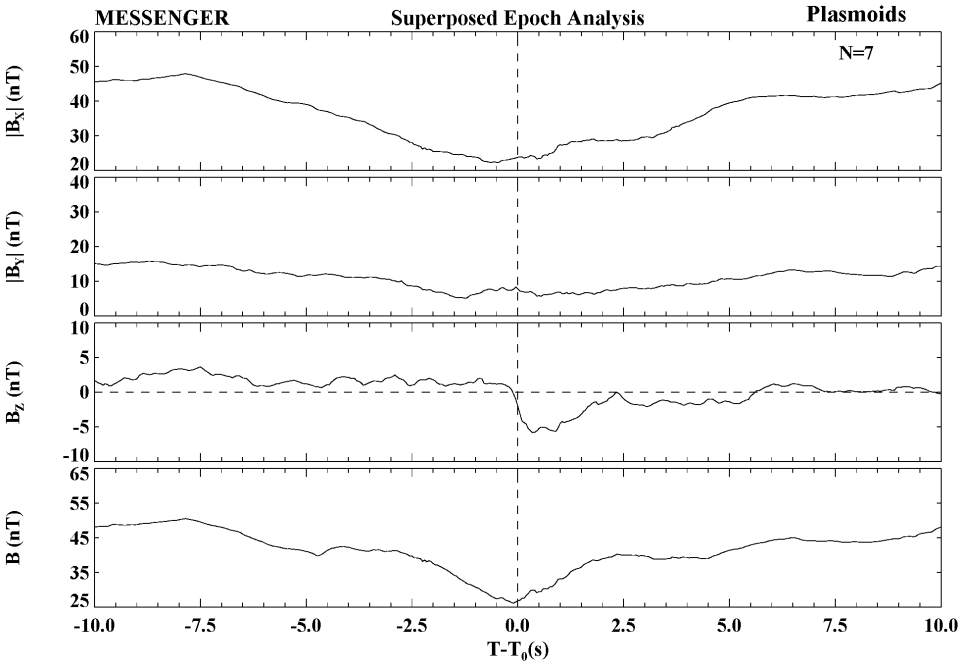

Figure 8a. Superposed epoch analysis of the one M2 and six M3 plasmoids over a ±10 s window. The north-then-south magnetic field variation takes place on a time scale of ~2 s and is followed by a longer postplasmoid interval of southward magnetic field.

plasmoid followed by a ~4–5 s interval of plasma sheet with southward B_Z that recovers toward zero. The observation of such "postplasmoid plasma sheet" intervals is very common and attributed to continued lobe reconnection after the plasmoid has been formed and has started to move down the tail [*Richardson et al.*, 1987]. There is no enhancement of the B_Y component as would be expected if the plasmoids had the magnetic topology of flux ropes [*Moldwin and Hughes*, 1992]. Further, there is a minimum in the total magnetic field intensity consistent with these

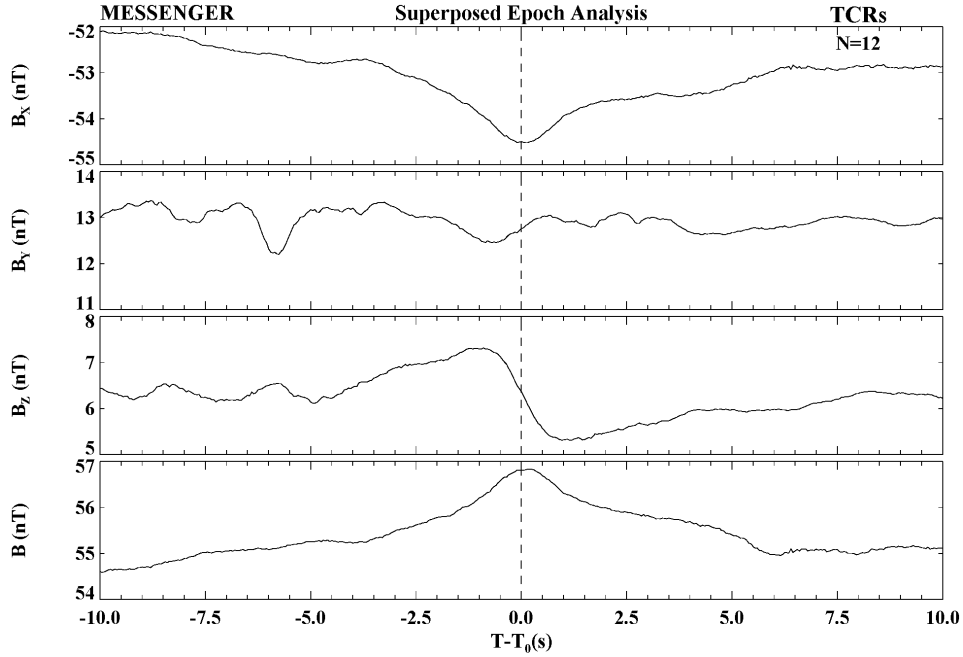

Figure 8b. Superposed epoch analysis of the nine M2 and three M3 traveling compression regions over a ±10 s window. The north-then-south tilting of the magnetic field and intensity enhancement occurs over a ~2 s interval. (Note that the times have been inverted for the SN TCRs to allow them to be summed with the NS events in this analysis.)

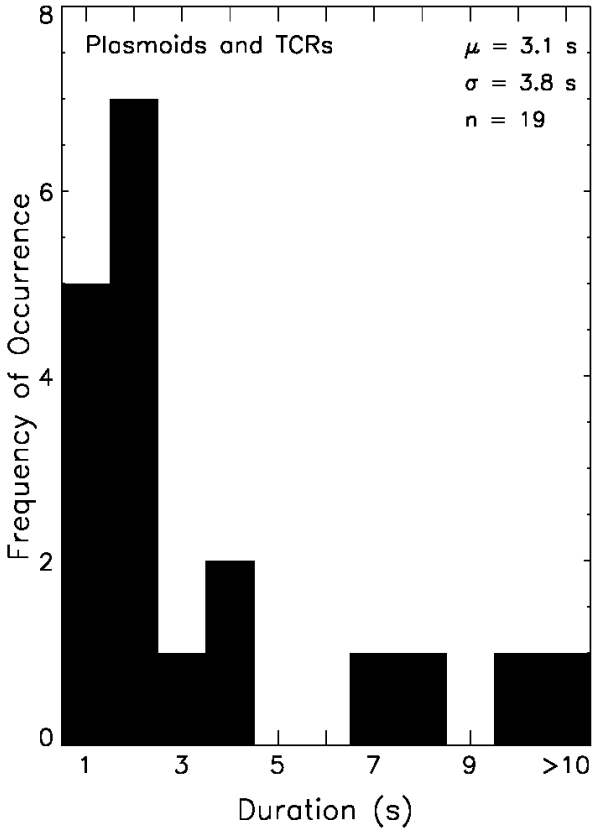

Figure 9a. Histogram of plasmoid and TCR duration derived from the times of the extreme excursions in ΔB_Z. The mean duration is 3.1 s.

MESSENGER plasmoids having a looplike as opposed to flux-rope-type magnetic structure. However, the number of plasmoids observed during the MESSENGER flybys is small. For this reason the apparent tendency toward more looplike as opposed to flux-rope-type plasmoids at Mercury requires confirmation from measurements made during MESSENGER's orbital mission phase.

[24] The superposed epoch analysis of the nine M2 and three M3 TCRs is presented in Figure 8b. Note that the relative times of the SN TCR magnetic field measurements have been reversed so that all 12 TCRs could be used to construct the superposed epoch-averaged NS waveform. The duration of the TCR perturbation is ~2–3 s, as was the case for the plasmoids. The compression ratio or amplitude of the variation in total magnetic field intensity for the Mercury TCRs was ~1 nT, or ~2% of the mean tail field. These values compare to a mean duration and amplitude of 36 s and 2.5% [*Slavin et al.*, 2005] for TCRs in Earth's tail at similar relative distances, respectively. Thus, the amplitudes of the TCRs in these two magnetospheres are quite similar, but their temporal durations are different by a factor of ~20.

[25] The durations of all of the M2 and M3 plasmoids and TCRs determined from the extrema in their B_Z and B_Y variations are displayed as a histogram in Figure 9a. The mean duration of the plasmoids and TCRs seen to date at Mercury was 3.1 s. The locations of the events are plotted along MESSENGER's M2 and M3 trajectories in Figure 9b. The transition from NS to SN events provides an average location of the dominant reconnection X lines [*Slavin et al.*, 2003, 2005]. The locations and polarities of the M2 and M3 events in Figure 9b indicate mean near-Mercury neutral line locations of $X'_{MSO} = -2.8\ R_M$ and $-1.8\ R_M$ for M2 and M3, respectively.

7. Determination of Plasma β for Plasma Sheet and Plasmoids

[26] The region of overlap between the Mariner 10 MI and MESSENGER M1 measurements in Figure 4a, $X' \sim -1.85$ to $-1.55\ R_M$, shows that the lobe magnetic field was a factor of ~2.5 greater than that in the central plasma sheet. If plasma pressure is negligible in the tail lobes, then from the balance of pressure between the lobe and plasma sheet, the ratio of plasma thermal pressure to magnetic pressure, $\beta = nk_B(T_i + T_e)/(B^2/2\mu_o)$, in the plasma sheet may be estimated from the magnetic field measurements alone:

$$\beta_{ps} = \left(B_L/B_{ps}\right)^2 - 1, \qquad (2)$$

where B_L and B_{ps} are the intensity of the magnetic fields in the lobes and plasma sheet, respectively, and where n, k_B, T_i, T_e, and μ_o are the ion density, Boltzmann constant, ion temperature, electron temperature, and magnetic permeability of free space, respectively. In this manner, the lobe and plasma sheet models in Figure 4a at $X' = -1.75\ R_M$ indicate a central plasma sheet β_{ps} value of ~5 for IMF $B_Z > 0$.

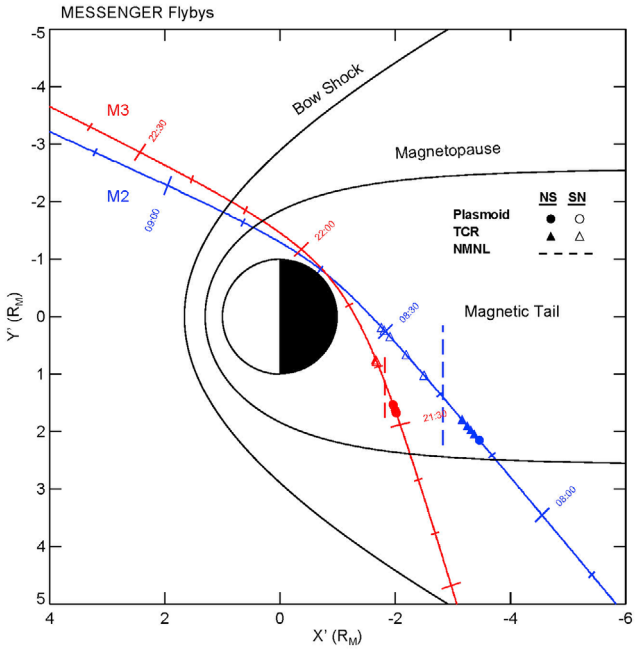

Figure 9b. MESSENGER M2 and M3 trajectories projected onto the aberrated X'_{MSO}–Y'_{MSO} plane with the locations of the sunward (SN) and tailward (NS) moving plasmoids (circles) and TCRs (triangles) indicated. Also shown as dashed lines are the mean locations of the near-Mercury neutral line during M2, $X' = -2.8\ R_M$, and M3, $X' = -1.8\ R_M$.

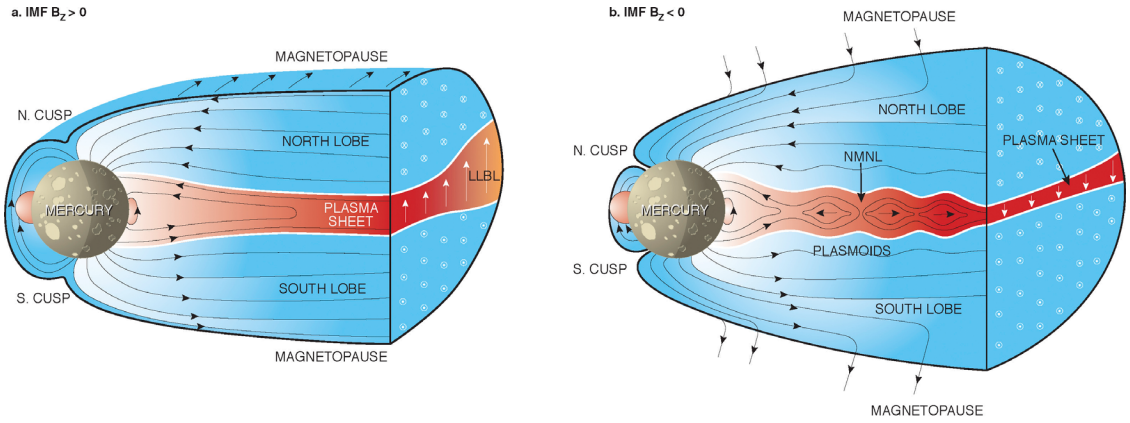

Figure 10. (a) Mercury's magnetosphere for IMF $B_Z > 0$ with no magnetic field normal to the magnetopause, limited flaring, a thick plasma sheet with no X lines, and a well-developed low-latitude boundary layer. (b) Under IMF $B_Z < 0$, dayside reconnection creates a strong magnetic field normal to the magnetopause, the dayside magnetosphere contracts as the cusps are displaced equatorward, the lobes load with magnetic flux, and the plasma sheet and embedded current sheet thin to the point of instability, leading to the development of the near-Mercury neutral line that dissipates the excess magnetic flux in the lobes.

[27] For IMF $B_Z < 0$, Figure 4b shows that we do not have simultaneous lobe and plasma sheet magnetic field measurements. However, each of the M3 plasmoids marked in Figure 6b was associated with a decrease in total magnetic field intensity, with the events beginning and ending with the spacecraft in the lobes of the tail. These rapid transitions from the lobe into the plasmoids can be used to infer plasma β within the plasmoids just as was done above for the plasma sheet. The β_{plasmoid} values for the six events in Figure 6b are 224, 148, 0.7, 2.6, 0.7, and 76. The lower β values for the third, fourth, and fifth plasmoids may be due to a shallower penetration of the spacecraft into the plasmoid. Indeed, the highest plasma β values were all associated with plasmoids for which MESSENGER observed the B_X component to approach zero and/or reverse sign, indicative of the spacecraft approaching or crossing the equatorial plane of the plasmoid where β would be expected to be highest.

8. Discussion

[28] MESSENGER's three flybys have returned new observations of Mercury's magnetotail between $X_{\text{MSO}} \sim -1.25$ and -3.25 R_M. For the modeled subsolar magnetopause distance of 1.3 R_M from the center of the planet [*Slavin et al.*, 2010b], these distances correspond to ~1–2.5 solar wind standoff distances. At Earth this number of standoff distances down the tail would correspond to $X \sim -11$ to -28 R_E. Alternatively, if we scale the MESSENGER flybys to the Earth's magnetosphere using a factor of ~8 on the basis of relative boundary locations [*Ogilvie et al.*, 1977], they would map to Earth-equivalent distances of $X \sim -12$ to -26 R_E in Earth's magnetotail. With either scaling approach, it is clear that the MESSENGER flyby measurements were taken in the region of the tail where experience at Earth would predict that magnetic reconnection is most frequently observed [*Nagai et al.*, 1998].

[29] The Mariner 10 and MESSENGER measurements show that the magnetic fields in Mercury's tail decrease with distance down the tail at a rate comparable to what is observed at Earth [*Nakai et al.*, 1999] and the other planets [*Kivelson and Khurana*, 2002; *Jackman and Arridge*, 2011]. The limited number of magnetopause boundary crossings available from the Mariner 10 and MESSENGER flybys is not yet sufficient to directly measure the enhanced flaring of this boundary as dayside reconnection adds magnetic flux to the tail lobes [cf. *Sibeck et al.*, 1991]. However, the lobe magnetic field intensities measured by Mariner 10 and MESSENGER at similar distances, $X \sim -1.65$ to -1.85 R_M, during steady northward and southward IMF are ~50 nT (MI) versus ~60 nT (M2), respectively. This observation of somewhat stronger lobe magnetic fields for southward IMF may be due to the expected increase in tail flaring in response to dayside magnetopause reconnection at Mercury, but changes in external solar wind pressure may also have occurred. The power law rate of decrease in the tail magnetic fields is more rapid for IMF $B_Z > 0$ than for $B_Z < 0$. This result is consistent with plasma sheet thinning and a reduction in the amount of magnetic field closing across the tail current sheet when the southward IMF and the tail stress levels are high.

[30] For none of the magnetic field profiles do the data suggest that the magnetic fields had reached their terminal value and ceased decreasing by $X'_{\text{MSO}} \sim -3.25$ R_M. If the ~100 R_E distance in the Earth's tail where magnetopause flaring ceases is scaled to Mercury using the factor of ~8 factor given by *Ogilvie et al.* [1977], then the resulting value is ~12.5 R_M, or about 4 times farther than the most distant tail measurements collected at Mercury to date. Hence, the fact that the Figure 4 lobe magnetic field profiles decrease throughout the domain $X' \sim -1.25$ to -3.25 R_M is consistent with expectations from Earth's tail.

[31] Examination of the flyby magnetic field measurements as a function of Y'_{MSO} has revealed the presence of a low-latitude boundary layer along the flanks of the tail. The great extent of the LLBL is shown approximately to scale in Figure 10a. Mercury's LLBL was observed to be thickest, $\sim 2 \times 10^3$ km or 0.8 R_M, during the M1 flyby with its steady, northward IMF. The LLBL was also present under variable-polarity IMF B_Z, during M3, but was thinner by a factor of

~2. It was completely absent for steady, southward IMF during M2. Statistical analyses of the tail magnetic field at Earth indicate that the width of the LLBL is typically 10%–20% of the radius of the magnetotail [*Fairfield*, 1979; *Slavin et al.*, 1985; *Kaymaz et al.*, 1994]. With LLBL thicknesses of ~33% and 16% of the mean magnetotail radius, the MESSENGER measurements suggest that the boundary layer at Mercury may be relatively greater in thickness than at Earth.

[32] The LLBL on the flanks of the tail is believed to arise as a result of quasi-viscous interactions between the solar wind and the geomagnetic field and/or double lobe reconnection [*Crooker*, 1979]. This latter reconnection-driven process splices segments of IMF flux tubes into planetary flux tubes by simultaneous reconnection at the northern and southern magnetic cusps [*Raeder et al.*, 1995]. The LLBLs seen during M1 and M3 also overlap with maxima in the flux of heavy planetary ions as measured by FIPS and with Kelvin-Helmholtz boundary wave activity [*Zurbuchen et al.*, 2008; *Slavin et al.*, 2008, 2010b; *Boardsen et al.*, 2010; *Sundberg et al.*, 2010]. Finite Larmor-radius effects associated with these heavy planetary ions are likely to play a role in the Kelvin-Helmholtz mechanism and other processes affecting the LLBL [*Uritsky et al.*, 2011]. The entry into the tail of planetary ions picked up in the magnetosheath would constitute a quasi-viscous process in that antisunward momentum is transmitted to the closed magnetic field lines along the flanks of Mercury's magnetosphere. Similarly, Kelvin-Helmholtz boundary waves propagating antisunward also result in the transfer of solar wind plasma and momentum to the closed magnetic flux tubes at the flanks of the magnetosphere [*Otto and Fairfield*, 2000; *Hasegawa et al.*, 2004; *Nakamura et al.*, 2006]. However, the fact that the MESSENGER observations of the LLBL were strongest for steady, northward IMF is also in good agreement with the double-cusp reconnection model for LLBL formation [*Raeder et al.*, 1995]. Additional measurements from MESSENGER's orbital phase will be necessary to determine whether Mercury's tail-flank LLBL is primarily controlled by cusp reconnection or whether Kelvin-Helmholtz boundary waves and/or planetary ions also play a role.

[33] The southward IMF during M2 produced steady tail magnetic fields whereas the variable-polarity IMF B_Z during M3 gave rise to a series of tail loading and unloading events. Each of these events lasted several minutes (see Figure 4b) and possessed relative amplitudes about an order of magnitude larger than observed at Earth [*Slavin et al.*, 2010b]. The frequent episodes of reconnection during the M2 and M3 tail passes was also evident in the plasmoids and TCRs recorded in the Magnetometer observations. The M2 plasmoids and TCRs were observed throughout the tail pass and were often separated in time from each other by ~30–60 s. Remarkably, the time separation between the two FTEs observed near the M2 magnetopause was also ~30 s [*Slavin et al.*, 2010a]. This separation raises the possibility that ~30 s is a fundamental time scale for more than one dynamic magnetospheric process at Mercury or that the magnetic flux transferred into the magnetotail by FTEs may be triggering the episodes of tail reconnection that produce the plasmoids and TCRs at ~30 s intervals.

[34] The plasmoids and TCRs during M3, in contrast with those seen during M2, were observed only near the time of peak tail loading. The six M3 plasmoids were also different in that they occurred in three pairs, with the plasmoids in each pair separated from each other by only a few seconds. However, the pairs were, in turn, separated from each other by ~30–60 s. The brief separations between the plasmoids in each pair argue that the two plasmoids formed simultaneously. Although formation in series cannot be ruled out by these single-spacecraft observations, it should be noted that the formation of "chains" of magnetic islands (i.e., plasmoids or flux ropes) is a well-known property of ion tearing-mode reconnection theory and simulation [*Schindler*, 1974; *Tanaka et al.*, 2011].

[35] The analysis of the events presented here indicates that the durations of the plasmoids and TCRs for M2 and M3 were ~1–3 s (see Figure 9a). At Earth the mean ejection speed for plasmoids is ~500 km/s [*Ieda et al.*, 1998; *Slavin et al.*, 2003]. Plasmoid ejection has also been observed at Jupiter [*Kronberg et al.*, 2008] and Saturn [*Hill et al.*, 2008] with Earth-like speeds of ~500–800 km/s. If we assume a similar plasmoid speed of 500 km/s at Mercury, then the average diameters of these structures at Mercury are ~500–1500 km, or 0.2–0.6 R_M. For the factor of ~8 spatial scaling from Mercury to Earth, these plasmoids documented by MESSENGER are similar in diameter to those observed in Earth's near-tail region [*Ieda et al.*, 1998; *Slavin et al.*, 2003]. These Mercury plasmoids and TCRs are depicted approximately to scale relative to Mercury and its magnetosphere in Figure 10b.

[36] Invoking pressure balance between the lobes and the plasma sheet, the ratio of the plasma thermal pressure to magnetic pressure has been inferred from the diamagnetic decrease in the magnetic field as the spacecraft moved from the lobe to plasma sheet and lobe to plasmoids. For IMF $B_Z > 0$, the MI and M1 magnetic field profiles imply a plasma sheet β_{ps} of ~5, which is comparable to what was determined for this region from H^+ plasma ion measurements by FIPS [*Raines et al.*, 2011]. It is also very near the average plasma β determined by *Slavin et al.* [1985] for Earth's plasma sheet between $X \sim -50$ and -220 R_E. However, the strongest diamagnetic decreases in magnetic field intensity were observed during the second M3 tail-loading event in association with transitions from the lobe region into plasmoids (see Figures 4b and 6b). In these cases β values up to ~224 are inferred from the magnetic field measurements. Plasma sheet β at Earth during reconnection events and in the vicinity of plasmoids is typically high, i.e., >1, with peak values of order 10^1 to 10^2, similar to those inferred from the MESSENGER measurements [*Frank et al.*, 1994; *Slavin et al.*, 2003; *Henderson et al.*, 2006; *Zhang et al.*, 2007]. These results indicating that reconnection produces strong heating of the magnetotail plasma populations at Mercury strongly support the factor of 20 increase in β in the near-tail plasma sheet determined by FIPS during M1 and M2 [*Raines et al.*, 2011].

[37] It has been shown that the sense of the plasmoid and TCR B_Z signatures changed from north-then-south to south-then-north tilting of the magnetic field at $X'_{MSO} = -2.8$ R_M and -1.8 R_M for M2 and M3, respectively. Just as at Earth [*Baker et al.*, 1996], this point where the plasma sheet flow, and the transport of plasmoids, changes from sunward to tailward is expected to correspond to the location of the near-Mercury neutral line (NMNL). Magnetic loops or flux ropes forming as a result of reconnection sunward of the

NMNL will be carried sunward toward Mercury, whereas structures forming antisunward of the NMNL will be ejected down the tail. The loops or flux ropes transported sunward are expected to dissipate by re-reconnecting with the stronger dipolar planetary magnetic field closer to the planet [*Slavin et al.*, 2003]. The antisunward plasmoids move down the tail at relatively high speed and are eventually lost to the solar wind [*Hones et al.*, 1984; *Moldwin and Hughes*, 1992; *Ieda et al.*, 1998]. These MESSENGER flyby observations support the arguments by *Baker et al.* [1986], from their analysis of the Mariner 10 energetic-particle events, that the NMNL forms very close to Mercury.

[38] The first, second, and third MESSENGER flybys occurred during steady northward, steady southward, and variable-polarity interplanetary magnetic field B_Z, respectively. Each of these IMF orientations is known to produce distinct magnetospheric responses in Earth's magnetosphere. The energy transferred to the terrestrial magnetosphere as a result of dayside reconnection can either be dissipated in a continuous manner, termed steady magnetospheric convection [*Sergeev et al.*, 1996], or loaded into the tail in the form of enhanced lobe magnetic field fields and then unloaded by tail reconnection during a substorm [*McPherron et al.*, 1973; *Baker et al.*, 1996]. The SMCs tend to develop during intervals of steady, moderate-intensity, southward IMF lasting many Dungey cycle times [*O'Brien et al.*, 2002; *Kissinger et al.*, 2010]. The duration of the tail loading and unloading intervals, sometimes referred to as the "growth" and "expansion" phases of the substorm because of the accompanying auroral signatures [*McPherron et al.*, 1973], are typically on the order of the Dungey cycle time. When the IMF B_Z polarity varies on time scales approaching the Dungey cycle time, isolated substorms with well-defined loading and unloading are observed [*Baker et al.*, 1996]. However, a strongly southward IMF B_Z can produce periodic substorms with very strong ~1–3 h long loading and unloading cycles with amplitudes of ~10% to 30% [*Huang and Cai*, 2009]. The amplitude of the tail loading and unloading observed by MESSENGER during M3 are nearly an order of magnitude larger than these most intense events at Earth [*Slavin et al.*, 2010b]. The fact that such strong tail loading can occur despite the very fast time scales for plasma and magnetic flux circulation within Mercury's magnetosphere is surprising [*Luhmann et al.*, 1998]. However, we speculate that the intensity of the loading of Mercury's tail may simply be a consequence of the very short time to transport flux from the dayside magnetopause into the tail, i.e., ~2 R_M/500 km/s = 10 s, relative to the ~2 min Dungey cycle time and the very high magnetopause reconnection rates. Although the lack of an ionosphere at Mercury contributes to the brief Dungey cycle, the rate of reconnection at Mercury's magnetopause may be higher still and result in major reconfigurations of this small magnetosphere [*Slavin and Holzer*, 1979; *Baker et al.*, 1986].

9. Summary

[39] Taken together, the results of this paper indicate that Mercury's magnetotail is structurally similar to that of Earth, at least under the average to weak solar wind conditions seen during the MESSENGER flybys [*Baker et al.*, 2009, 2011]. It responds to IMF direction in a manner qualitatively similar to Earth's tail, but with much shorter time scales and greater intensity. Steady northward IMF produces steady lobe magnetic fields, a relatively low-β plasma sheet, and thick low-latitude boundary layers and Kelvin-Helmholtz boundary waves at the flanks of the tail. Steady southward IMF causes tail reconnection to take place in a continuous but episodic manner without marked loading and unloading of the lobes. Further, the observed quasiperiodic ejection of plasmoids down the tail appears to remove or suppress the development of the closed field-line flank LLBL. Variable polarity IMF B_Z, especially on time scales comparable to Mercury's Dungey cycle, produces large-amplitude, substorm-like tail loading and unloading, a high-β plasma sheet, reconnection X line formation very close to Mercury, and plasmoid ejection around the time of peak tail loading. Although not treated here, MESSENGER did observe clear evidence for plasma electron acceleration and heating during the flybys, but not above the cross-magnetospheric potential of ~30 keV [*Slavin et al.*, 2009; *Ho et al.*, 2011].

[40] The analysis of the MESSENGER magnetic field observations taken during the three flybys have laid a foundation for the orbital phase investigations to follow, but they leave open many of the most important questions. These include (1) the number density, degree of thermalization, and spatial distribution of the heavy planetary ion populations known to exist at Mercury [*Ip*, 1987; *Delcourt et al.*, 2003; *Zurbuchen et al.*, 2008; *Vervack et al.*, 2010; *Paral et al.*, 2010; *Yagi et al.*, 2010]; (2) the nature of the electrodynamic coupling of the high-altitude magnetosphere to Mercury [*Lyatsky et al.*, 2010]; (3) the primary mechanism and properties of energetic particle acceleration within Mercury's magnetosphere [*Schriver et al.*, 2011]; and (4) the final reconciliation of the Mariner 10 energetic electron acceleration events with the much weaker acceleration and heating observed by MESSENGER [*Baker et al.*, 1986; *Christon et al.*, 1987; *Ho et al.*, 2011]. Further observations from orbit about Mercury are needed to make further progress on these open issues.

[41] **Acknowledgments.** Computational assistance and data visualization support provided by J. Feggans are gratefully acknowledged. We are also pleased to acknowledge stimulating comments and discussions with V. Uritsky. The MESSENGER project is supported by the NASA Discovery Program under contracts NASW-00002 to the Carnegie Institution of Washington and NAS5-97271 to the Johns Hopkins University Applied Physics Laboratory.

[42] Masaki Fujimoto thanks Lars Blomberg and another reviewer for their assistance in evaluating this paper.

References

Alexeev, I. I., E. S. Belenkaya, S. Y. Bobrovnikov, J. A. Slavin, and M. Sarantos (2008), Paraboloid model of Mercury's magnetosphere, *J. Geophys. Res.*, *113*, A12210, doi:10.1029/2008JA013368.

Alexeev, I. I., et al. (2010), Mercury's magnetospheric magnetic field after the first two MESSENGER flybys, *Icarus*, *209*, 23–39, doi:10.1016/j.icarus.2010.01.024.

Anderson, B. J., M. H. Acuña, D. A. Lohr, J. Scheifele, A. Raval, H. Korth, and J. A. Slavin (2007), The Magnetometer instrument on MESSENGER, *Space Sci. Rev.*, *131*, 417–450, doi:10.1007/s11214-007-9246-7.

Anderson, B. J., M. H. Acuña, H. Korth, M. E. Purucker, C. L. Johnson, J. A. Slavin, S. C. Solomon, and R. L. McNutt Jr. (2008), The structure of Mercury's magnetic field from MESSENGER's first flyby, *Science*, *321*, 82–85, doi:10.1126/science.1159081.

Anderson, B. J., et al. (2010), The magnetic field of Mercury, *Space Sci. Rev.*, *152*, 307–339, doi:10.1007/s11214-009-9544-3.

Anderson, B. J., J. A. Slavin, H. Korth, S. A. Boardsen, T. H. Zurbuchen, J. M. Raines, G. Gloeckler, R. L. McNutt Jr., and S. C. Solomon (2011),

The dayside magnetospheric boundary layer at Mercury, *Planet. Space Sci.*, *59*, 2037–2050, doi:10.1016/j.pss.2011.01.010.

Baker, D. N., J. A. Simpson, and J. H. Eraker (1986), A model of impulsive acceleration and transport of energetic particles in Mercury's magnetosphere, *J. Geophys. Res.*, *91*, 8742–8748, doi:10.1029/JA091iA08p08742.

Baker, D. N., T. I. Pulkkinen, V. Angelopoulos, W. Baumjohann, and R. L. McPherron (1996), Neutral line model of substorms: Past results and present view, *J. Geophys. Res.*, *101*, 12,975–13,010, doi:10.1029/95JA03753.

Baker, D. N., et al. (2009), Space environment of Mercury at the time of the first MESSENGER flyby: Solar wind and interplanetary magnetic field modeling of upstream conditions, *J. Geophys. Res.*, *114*, A10101, doi:10.1029/2009JA014287.

Baker, D. N., et al. (2011), The space environment of Mercury at the time of the second and third MESSENGER flybys, *Planet. Space Sci.*, *59*, 2066–2074, doi:10.1016/j.pss.2011.01.018.

Baumjohann, W., et al. (2006), The magnetosphere of Mercury and its solar wind environment: Open issues and scientific questions, *Adv. Space Res.*, *38*, 604–609, doi:10.1016/j.asr.2005.05.117.

Benna, M., et al. (2010), Modeling of the magnetosphere of Mercury at the time of the first MESSENGER flyby, *Icarus*, *209*, 3–10, doi:10.1016/j.icarus.2009.11.036.

Boardsen, S. A., T. Sundberg, J. A. Slavin, B. J. Anderson, H. Korth, S. C. Solomon, and L. G. Blomberg (2010), Observations of Kelvin-Helmholtz waves along the dusk-side boundary of Mercury's magnetosphere during MESSENGER's third flyby, *Geophys. Res. Lett.*, *37*, L12101, doi:10.1029/2010GL043606.

Caan, M. N., R. L. McPherron, and C. T. Russell (1973), Solar wind and substorm-related changes in the lobes of the geomagnetic tail, *J. Geophys. Res.*, *78*, 8087–8096, doi:10.1029/JA078i034p08087.

Christon, S. P., J. Feynman, and J. A. Slavin (1987), Substorm injection fronts: Similar magnetospheric phenomena at Earth and Mercury, in *Magnetotail Physics*, edited by A. T. Y. Lui, pp. 393–402, Johns Hopkins Univ. Press, Baltimore, Md.

Coroniti, F. V., and C. F. Kennel (1972), Changes in magnetospheric configuration during the substorm growth phase, *J. Geophys. Res.*, *77*, 3361–3370, doi:10.1029/JA077i019p03361.

Cowley, S. W. H. (1982), The causes of convection in the Earth's magnetosphere: A review of developments during the IMS, *Rev. Geophys.*, *20*, 531–565, doi:10.1029/RG020i003p00531.

Crooker, N. U. (1979), Dayside merging and cusp geometry, *J. Geophys. Res.*, *84*, 951–959, doi:10.1029/JA084iA03p00951.

Delcourt, D. C., S. Grimald, F. Leblanc, J.-J. Bethelier, A. Millilo, A. Mura, S. Orisini, and T. E. Moore (2003), A quantitative model of the planetary Na^+ contribution to Mercury's magnetosphere, *Ann. Geophys.*, *21*, 1723–1736, doi:10.5194/angeo-21-1723-2003.

Dungey, J. W. (1961), Interplanetary magnetic field and the auroral zones, *Phys. Rev. Lett.*, *6*, 47–48, doi:10.1103/PhysRevLett.6.47.

Fairfield, D. H. (1979), On the average configuration of the geomagnetic tail, *J. Geophys. Res.*, *84*, 1950–1958, doi:10.1029/JA084iA05p01950.

Frank, L. A., W. R. Paterson, K. L. Ackerson, S. Kokubun, T. Yamamoto, D. H. Fairfield, and R. P. Lepping (1994), Observations of plasmas associated with the magnetic signature of a plasmoid in the distant magnetotail, *Geophys. Res. Lett.*, *21*, 2967–2970, doi:10.1029/94GL01604.

Fujimoto, M., W. Baumjohann, K. Kabin, R. Nakamura, J. A. Slavin, N. Terada, and L. Zelenyi (2007), Hermean magnetosphere-solar wind interaction, *Space Sci. Rev.*, *132*, 529–550, doi:10.1007/s11214-007-9245-8.

Hasegawa, H., M. Fujimoto, T.-D. Phan, H. Rème, A. Balogh, M. W. Dunlop, C. Hashimoto, and R. TanDokoro (2004), Transport of solar wind into Earth's magnetosphere through rolled-up Kelvin-Helmholtz vortices, *Nature*, *430*, 755–758, doi:10.1038/nature02799.

Henderson, M. G., G. D. Reeves, R. D. Belian, and J. S. Murphy (1996), Observations of magnetospheric substorms with no apparent solar wind/IMF trigger, *J. Geophys. Res.*, *101*, 10,773–10,791, doi:10.1029/96JA00186.

Henderson, P. D., C. J. Owen, I. V. Alexeev, J. A. Slavin, N. Fazakerley, E. Lucek, and H. Rème (2006), Cluster observations of flux rope structures in the near-tail, *Ann. Geophys.*, *24*, 651–666, doi:10.5194/angeo-24-651-2006.

Hesse, M., and M. G. Kivelson (1998), The formation and structure of flux ropes in the magnetotail, in *New Frontiers in Magnetotail Research*, *Geophys. Monogr. Ser.*, vol. 105, edited by A. Nishida, D. N. Baker, and S. W. H. Cowley, pp. 139–147, AGU, Washington, D. C.

Hill, T. W., et al. (2008), Plasmoids in Saturn's magnetotail, *J. Geophys. Res.*, *113*, A01214, doi:10.1029/2007JA012626.

Ho, G. C., R. D. Starr, R. E. Gold, S. M. Krimigis, J. A. Slavin, D. N. Baker, B. J. Anderson, R. L. McNutt Jr., L. R. Nittler, and S. C. Solomon (2011), Observations of suprathermal electrons in Mercury's magnetosphere during the three MESSENGER flybys, *Planet. Space Sci.*, *59*, 2016–2025, doi:10.1016/j.pss.2011.01.011.

Hones, E. W., Jr., J. R. Asbridge, S. J. Bame, M. D. Montgomery, S. Singer, and S.-I. Akasofu (1972), Measurements of magnetotail plasma flow made with Vela 4B, *J. Geophys. Res.*, *77*, 5503–5522, doi:10.1029/JA077i028p05503.

Hones, E. W., Jr., D. N. Baker, S. J. Bame, W. C. Feldman, J. T. Gosling, D. J. McComas, R. D. Zwickl, J. A. Slavin, E. J. Smith, and B. T. Tsurutani (1984), Structure of the magnetotail at 220 R_E and its response to geomagnetic activity, *Geophys. Res. Lett.*, *11*, 5–7, doi:10.1029/GL011i001p00005.

Hsu, T.-S., and R. L. McPherron (2004), Average characteristics of triggered and non-triggered substorms, *J. Geophys. Res.*, *109*, A07208, doi:10.1029/2003JA009933.

Huang, C.-S., and X. Cai (2009), Magnetotail total pressure and lobe magnetic field at onsets of sawtooth events and their relation to the solar wind, *J. Geophys. Res.*, *114*, A04204, doi:10.1029/2008JA013807.

Ieda, A., S. Machida, T. Mukai, Y. Saito, T. Yamamoto, A. Nishida, T. Teresawa, and S. Kokubun (1998), Statistical analysis of plasmoid evolution with GEOTAIL observations, *J. Geophys. Res.*, *103*, 4453–4465, doi:10.1029/97JA03240.

Ip, W.-H. (1987), Dynamics of electrons and heavy ions in Mercury's magnetosphere, *Icarus*, *71*, 441–447, doi:10.1016/0019-1035(87)90039-X.

Ip, W.-H., and A. Kopp (2002), MHD simulation of the solar wind interaction with Mercury, *J. Geophys. Res.*, *107*(A11), 1348, doi:10.1029/2001JA009171.

Jackman, C. M., and C. S. Arridge (2011), Statistical properties of the magnetic field in the Kronian magnetotail lobes and current sheet, *J. Geophys. Res.*, *116*, A05224, doi:10.1029/2010JA015973.

Janhunen, P., and E. Kallio (2004), Surface conductivity of Mercury provides current closure and may affect magnetospheric symmetry, *Ann. Geophys.*, *22*, 1829–1837, doi:10.5194/angeo-22-1829-2004.

Kabin, K., T. I. Gombosi, D. L. DeZeeuw, and K. G. Powell (2000), Interaction of Mercury with the solar wind, *Icarus*, *143*, 397–406, doi:10.1006/icar.1999.6252.

Kaymaz, Z., G. L. Siscoe, J. G. Luhmann, R. P. Lepping, and C. T. Russell (1994), Interplanetary magnetic field control of magnetotail magnetic geometry: IMP 8 observations, *J. Geophys. Res.*, *99*, 11,113–11,126, doi:10.1029/94JA00300.

Kidder, A., R. M. Winglee, and E. M. Harnett (2008), Erosion of the dayside magnetosphere at Mercury in association with ion outflows and flux rope generation, *J. Geophys. Res.*, *113*, A09223, doi:10.1029/2008JA013038.

Kissinger, J., R. L. McPherron, V. Angelopoulos, T.-S. Hsu, and J. P. McFadden (2010), An investigation of the association between steady magnetospheric convection and CIR stream interfaces, *Geophys. Res. Lett.*, *37*, L04105, doi:10.1029/2009GL041541.

Kivelson, M. G., and K. K. Khurana (2002), Properties of the magnetic field in the Jovian magnetotail, *J. Geophys. Res.*, *107*(A8), 1196, doi:10.1029/2001JA000249.

Korth, H., B. J. Anderson, T. H. Zurbuchen, J. A. Slavin, S. Perri, S. A. Boardsen, D. N. Baker, S. C. Solomon, and R. L. McNutt Jr. (2011), The interplanetary magnetic field environment at Mercury's orbit, *Planet. Space Sci.*, *59*, 2075–2085, doi:10.1016/j.pss.2010.10.014.

Kronberg, E. A., J. Woch, N. Krupp, and A. Lagg (2008), Mass release process in the Jovian magnetosphere: Statistics on particle burst parameters, *J. Geophys. Res.*, *113*, A10202, doi:10.1029/2008JA013332.

Kuznetsova, M. M., M. Hesse, L. Rastaetter, A. Taktakishvili, G. Toth, D. L. D. Zeeuw, A. Ridley, and T. I. Gombosi (2007), Multiscale modeling of magnetospheric reconnection, *J. Geophys. Res.*, *112*, A10210, doi:10.1029/2007JA012316.

Liou, K. (2007), Large, abrupt pressure decreases as a substorm onset trigger, *Geophys. Res. Lett.*, *34*, L14107, doi:10.1029/2007GL029909.

Luhmann, J. G., C. T. Russell, and N. A. Tsyganenko (1998), Disturbances in Mercury's magnetosphere: Are the Mariner 10 "substorms" simply driven?, *J. Geophys. Res.*, *103*, 9113–9119, doi:10.1029/97JA03667.

Lyatsky, W., G. V. Khazanov, and J. A. Slavin (2010), Alfven wave reflection model of field-aligned currents at Mercury, *Icarus*, *209*, 40–45, doi:10.1016/j.icarus.2009.11.039.

Lyons, L. R., G. T. Blanchard, J. C. Samson, R. P. Lepping, T. Yamamoto, and T. Moretto (1997), Coordinated observations demonstrating external substorm triggering, *J. Geophys. Res.*, *102*, 27,039–27,051, doi:10.1029/97JA02639.

Macek, W., and S. Grzedzielski (1986), Planetary magnetotails: Model based on ISEE-3 and Voyager 2 evidence, *Adv. Space Res.*, *6*, 283–289, doi:10.1016/0273-1177(86)90044-X.

McPherron, R. L., C. T. Russell, and M. P. Aubry (1973), Satellite studies of magnetospheric substorms on August 15, 1968, 9, Phenomenological model for substorms, *J. Geophys. Res.*, *78*, 3131–3149, doi:10.1029/JA078i016p03131.

McPherron, R. L., T. P. O'Brien, and S. Thompson (2005), Solar wind drivers for steady magnetospheric convection, in *Multiscale Coupling*

of Sun-Earth Processes, edited by A. T. Y. Lui, Y. Kamide, and G. Consolini, pp. 113–124, Elsevier, New York, doi:10.1016/B978-044451881-1/50009-5.

Milan, S. E., S. W. H. Cowley, M. Lester, D. M. Wright, J. A. Slavin, M. Fillingim, C. W. Carlson, and H. J. Singer (2004), Response of the magnetotail to changes in the open flux content of the magnetosphere, *J. Geophys. Res.*, *109*, A04220, doi:10.1029/2003JA010350.

Mitchell, D. G., F. Kutchko, D. J. Williams, T. E. Eastman, L. A. Frank, and C. T. Russell (1987), An extended study of the low-latitude boundary layer on the dawn and dusk flanks of the magnetosphere, *J. Geophys. Res.*, *92*, 7394–7404, doi:10.1029/JA092iA07p07394.

Moldwin, M. B., and W. J. Hughes (1992), On the formation and evolution of plasmoids: A survey of the ISEE 3 Geotail data, *J. Geophys. Res.*, *97*, 19,259–19,282, doi:10.1029/92JA01598.

Nagai, T., M. Fujimoto, Y. Saito, S. Machida, T. Terasawa, R. Nakamura, T. Yamamoto, T. Mukai, A. Nishida, and S. Kokubun (1998), Structure and dynamics of magnetic reconnection for substorm onsets with Geotail observations, *J. Geophys. Res.*, *103*, 4419–4440, doi:10.1029/97JA02190.

Nakai, H., Y. Kamide, and C. T. Russell (1999), Dependence of the near-Earth magnetotail magnetic field on storm and substorm activities, *Geophys. Res. Lett.*, *104*, 22,701–22,711.

Nakamura, T. K. M., M. Fujimoto, and A. Otto (2006), Magnetic reconnection induced by weak Kelvin-Helmholtz instability and the formation of the low-latitude boundary layer, *Geophys. Res. Lett.*, *33*, L14106, doi:10.1029/2006GL026318.

Ness, N. F., K. W. Behannon, R. P. Lepping, Y. C. Wang, and K. H. Schatten (1974), Observations of magnetic field near Mercury: Preliminary results from Mariner 10, *Science*, *185*, 151–160, doi:10.1126/science.185.4146.151.

O'Brien, T. P., S. M. Thompson, and R. L. McPherron (2002), Steady magnetospheric convection: Statistical signatures in the solar wind and AE, *Geophys. Res. Lett.*, *29*(7), 1130, doi:10.1029/2001GL014641.

Ogilvie, K. W., J. D. Scudder, V. M. Vasyliunas, R. E. Hartle, and G. L. Siscoe (1977), Observations at the planet Mercury by the plasma electron experiment: Mariner 10, *J. Geophys. Res.*, *82*, 1807–1824, doi:10.1029/JA082i013p01807.

Otto, A., and D. H. Fairfield (2000), Kelvin-Helmholtz instability at the magnetotail boundary: MHD simulation and comparison with Geotail observations, *J. Geophys. Res.*, *105*, 21,175–21,190, doi:10.1029/1999JA000312.

Paral, J., P. M. Trávníček, R. Rankin, and D. Schriver (2010), Sodium ion exosphere of Mercury during MESSENGER flybys, *Geophys. Res. Lett.*, *37*, L19102, doi:10.1029/2010GL044413.

Raeder, J., R. J. Walker, and M. Ashour-Abdalla (1995), Magnetic flux ropes at the high-latitude magnetopause, *Geophys. Res. Lett.*, *22*, 349–352, doi:10.1029/94GL03380.

Raeder, J., P. Zhu, Y. Ge, and G. L. Siscoe (2010), Open Geospace General Circulation Model simulation of a substorm: Axial tail instability and ballooning mode preceding substorm onset, *J. Geophys. Res.*, *115*, A00I16, doi:10.1029/2010JA015876.

Raines, J. M., J. A. Slavin, T. H. Zurbuchen, G. Gloeckler, B. J. Anderson, D. N. Baker, H. Korth, S. M. Krimigis, and R. L. McNutt Jr. (2011), MESSENGER observations of the plasma environment near Mercury, *Planet. Space Sci.*, *59*, 2004–2015, doi:10.1016/j.pss.2011.02.004.

Richardson, I. G., S. W. H. Cowley, E. W. Hones Jr., and S. J. Bame (1987), Plasmoid-associated energetic ion bursts in the deep geomagnetic tail: Properties of plasmoids and the postplasmoid plasma sheet, *J. Geophys. Res.*, *92*, 9997–10,013, doi:10.1029/JA092iA09p09997.

Russell, C. T., D. N. Baker, and J. A. Slavin (1988), The magnetosphere of Mercury, in *Mercury*, edited by F. Vilas, C. R. Chapman, and M. S. Matthews, pp. 514–561, Univ. of Ariz. Press, Tucson.

Schindler, K. (1974), A theory of the substorm mechanism, *J. Geophys. Res.*, *79*, 2803–2810, doi:10.1029/JA079i019p02803.

Schriver, D., et al. (2011), Electron transport and precipitation at Mercury during the MESSENGER flybys: Implications for electron-stimulated desorption, *Planet. Space Sci.*, *59*, 2026–2036, doi:10.1016/j.pss.2011.03.008.

Sergeev, V. A., R. J. Pellinen, and T. I. Pulkkinen (1996), Steady magnetospheric convection: A review of recent results, *Space Sci. Rev.*, *75*, 551–604, doi:10.1007/BF00833344.

Sibeck, D. G., R. E. Lopez, and E. C. Roelof (1991), Solar wind control of the magnetopause shape, location, and motion, *J. Geophys. Res.*, *96*, 5489–5495, doi:10.1029/90JA02464.

Siscoe, G. L., N. F. Ness, and C. M. Yeates (1975), Substorms on Mercury?, *J. Geophys. Res.*, *80*, 4359–4363, doi:10.1029/JA080i031p04359.

Slavin, J. A. (2004), Mercury's magnetosphere, *Adv. Space Res.*, *33*, 1859–1874, doi:10.1016/j.asr.2003.02.019.

Slavin, J. A., and R. E. Holzer (1979), The effect of erosion on the solar wind stand-off distance at Mercury, *J. Geophys. Res.*, *84*, 2076–2082, doi:10.1029/JA084iA05p02076.

Slavin, J. A., E. J. Smith, D. G. Sibeck, D. N. Baker, R. D. Zwickl, and S.-I. Akasofu (1985), An ISEE-3 study of average and substorm conditions in the distant magnetotail, *J. Geophys. Res.*, *90*, 10,875–10,895, doi:10.1029/JA090iA11p10875.

Slavin, J. A., M. F. Smith, E. L. Mazur, D. N. Baker, T. Iyemori, H. J. Singer, and E. W. Greenstadt (1992), ISEE 3 plasmoid and TCR observations during an extended interval of substorm activity, *Geophys. Res. Lett.*, *19*, 825–828, doi:10.1029/92GL00394.

Slavin, J. A., M. F. Smith, E. L. Mazur, D. N. Baker, T. Iyemori, and E. W. Greenstadt (1993), ISEE-3 observations of traveling compression regions in the Earth's magnetotail, *J. Geophys. Res.*, *98*, 15,425–15,446, doi:10.1029/93JA01467.

Slavin, J. A., R. P. Lepping, J. Gjerloev, D. H. Fairfield, M. Hesse, C. J. Owen, M. B. Moldwin, T. Nagai, A. Ieda, and T. Mukai (2003), Geotail observations of magnetic flux ropes in the plasma sheet, *J. Geophys. Res.*, *108*(A1), 1015, doi:10.1029/2002JA009557.

Slavin, J. A., E. Tanskanen, M. Hesse, C. J. Owen, M. W. Dunlop, S. Imber, E. Lucek, A. Balogh, and K.-H. Glassmeier (2005), Cluster observations of traveling compression regions in the near-tail, *J. Geophys. Res.*, *110*, A06207, doi:10.1029/2004JA010878.

Slavin, J. A., et al. (2008), Mercury's magnetosphere after MESSENGER's first flyby, *Science*, *321*, 85–89, doi:10.1126/science.1159040.

Slavin, J. A., et al. (2009), MESSENGER observations of magnetic reconnection in Mercury's magnetosphere, *Science*, *324*, 606–610, doi:10.1126/science.1172011.

Slavin, J. A., et al. (2010a), MESSENGER observations of large flux transfer events at Mercury, *Geophys. Res. Lett.*, *37*, L02105, doi:10.1029/2009GL041485.

Slavin, J. A., et al. (2010b), MESSENGER observations of extreme loading and unloading of Mercury's magnetic tail, *Science*, *329*, 665–668, doi:10.1126/science.1188067.

Solomon, S. C., et al. (2001), The MESSENGER mission to Mercury: Scientific objectives and implementation, *Planet. Space Sci.*, *49*, 1445–1465, doi:10.1016/S0032-0633(01)00085-X.

Sundberg, T., S. A. Boardsen, J. A. Slavin, L. G. Blomberg, and H. Korth (2010), The Kelvin-Helmholtz instability at Mercury: An assessment, *Planet. Space Sci.*, *58*, 1434–1441, doi:10.1016/j.pss.2010.06.008.

Tanaka, K. G., M. Fujimoto, and I. Shinohara (2011), On the peak level of tearing instability in an ion-scale current sheet: The effects of ion temperature anisotropy, *Planet. Space Sci.*, *59*, 510–516, doi:10.1016/j.pss.2010.04.014.

Tanskanen, E., J. A. Slavin, D. H. Fairfield, D. G. Sibeck, J. Gjerloev, T. Mukai, A. Ieda, and T. Nagai (2005), Response of the magnetotail to prolonged southward B_z intervals: Loading, unloading, and continuous dissipation, *J. Geophys. Res.*, *110*, A03216, doi:10.1029/2004JA010561.

Trávníček, P. M., D. Schriver, P. Hellinger, D. Herčík, B. J. Anderson, M. Sarantos, and J. A. Slavin (2010), Mercury's magnetosphere–solar wind interaction for northward and southward interplanetary magnetic field: Hybrid simulations, *Icarus*, *209*, 11–22, doi:10.1016/j.icarus.2010.01.008.

Uritsky, V. M., J. A. Slavin, G. V. Khazanov, E. F. Donovan, S. A. Boardsen, B. J. Anderson, and H. Korth (2011), Kinetic-scale magnetic turbulence and finite Larmor radius effects at Mercury, *J. Geophys. Res.*, *116*, A09236, doi:10.1029/2011JA016744.

Vervack, R. J., Jr., W. E. McClintock, R. M. Killeen, A. L. Sprague, B. J. Anderson, M. H. Burger, E. T. Bradley, N. Mouawad, S. C. Solomon, and N. R. Izenberg (2010), Mercury's complex exosphere: Results from MESSENGER's third flyby, *Science*, *329*, 672–675, doi:10.1126/science.1188572.

Wang, Y.-C., J. Mueller, U. Motschmann, and W.-H. Ip (2010), A hybrid simulation of Mercury's magnetosphere for the MESSENGER encounters in year 2008, *Icarus*, *209*, 46–52, doi:10.1016/j.icarus.2010.05.020.

Winglee, R. M., E. Harnett, and A. Kidder (2009), Relative timing of substorm processes as derived from multifluid/multiscale simulations: Internally driven substorms, *J. Geophys. Res.*, *114*, A09213, doi:10.1029/2008JA013750.

Yagi, M., K. Seki, Y. Matsumoto, D. C. Delcourt, and F. Leblanc (2010), Formation of a sodium ring in Mercury's magnetosphere, *J. Geophys. Res.*, *115*, A10253, doi:10.1029/2009JA015226.

Zhang, Y. C., Z. X. Liu, C. Shen, A. Fazakerley, M. Dunlop, H. Rème, E. Lucek, A. P. Walsh, and L. Yao (2007), The magnetic structure of an earthward-moving flux rope observed by Cluster in the near-tail, *Ann. Geophys.*, *25*, 1471–1476, doi:10.5194/angeo-25-1471-2007.

Zurbuchen, T. H., J. M. Raines, G. Gloeckler, S. M. Krimigis, J. A. Slavin, P. L. Koehn, R. M. Killen, A. L. Sprague, R. L. McNutt Jr., and S. C. Solomon (2008), MESSENGER observations of the composition of

Mercury's ionized exosphere and plasma environment, *Science*, *321*, 90–92, doi:10.1126/science.1159314.

B. J. Anderson, R. E. Gold, G. C. Ho, H. Korth, S. M. Krimigis, and R. L. McNutt Jr., Johns Hopkins University Applied Physics Laboratory, 11100 Johns Hopkins Rd., Laurel, MD 20723, USA.

D. N. Baker, Laboratory for Solar and Atmospheric Physics, University of Colorado at Boulder, 1234 Innovation Dr., Boulder, CO 80303, USA.

M. Benna, Solar System Exploration Division, NASA Goddard Space Flight Center, Code 699, Greenbelt, MD 20771, USA.

S. A. Boardsen, S. M. Imber, M. Sarantos, and J. A. Slavin, Heliophysics Science Division, NASA Goddard Space Flight Center, Code 670.0, Bldg. 21, Greenbelt Road, Greenbelt, MD 20771, USA.

J. M. Raines and T. H. Zurbuchen, Department of Atmospheric, Oceanic and Space Sciences, 2455 Hayward St., University of Michigan, Ann Arbor, MI 48109, USA.

D. Schriver, Institute for Geophysics and Planetary Physics, University of California, 3871 Slichter Hall, Box 951567, Los Angeles, CA 90024, USA.

S. C. Solomon, Department of Terrestrial Magnetism, Carnegie Institution of Washington, 5241 Broad Branch Rd. NW, Washington, DC 20015, USA.

P. Trávníček, Astronomical Institute, Academy of Sciences of the Czech Republic, 14131 Prague, Czech Republic.